Icarus 252 (2015) 284–300

Contents lists available at ScienceDirect

Icarus

journal homepage: www.elsevier.com/locate/icarus

Remote detection of past habitability at Mars-analogue hydrothermal alteration terrains using an ExoMars Panoramic Camera emulator

J.K. Harris [a,b,*], C.R. Cousins [c,d], M. Gunn [e], P.M. Grindrod [a,b], D. Barnes [e], I.A. Crawford [a,b], R.E. Cross [e], A.J. Coates [f]

[a] Department of Earth and Planetary Sciences, Birkbeck, University of London, London WC1E 7HX, UK
[b] UCL/BBK Centre for Planetary Sciences, University College London, London WC1E 6BT, UK
[c] UK Centre for Astrobiology, University of Edinburgh, Edinburgh EH9 3JZ, UK
[d] School of Physics and Astronomy, University of Edinburgh, Edinburgh EH9 3JZ, UK
[e] Institute of Mathematics, Physics and Computer Science (IMPACS), Aberystwyth University, Aberystwyth SY23 3BZ, UK
[f] Mullard Space Science Laboratory, University College London, Dorking, Surrey RH5 6NT, UK

ARTICLE INFO

Article history:
Received 15 May 2014
Revised 14 January 2015
Accepted 1 February 2015
Available online 10 February 2015

This paper is dedicated to the late Prof. Dave Barnes who sadly passed away before the publication of this work, to which he had significantly contributed over the years through his work on the ExoMars PanCam.

Keywords:
Mars, surface
Mineralogy
Spectroscopy
Astrobiology
Instrumentation

ABSTRACT

A major scientific goal of the European Space Agency's ExoMars 2018 rover is to identify evidence of life within the martian rock record. Key to this objective is the remote detection of geological substrates that are indicative of past habitable environments, which will rely on visual (stereo wide-angle, and high resolution images) and multispectral (440–1000 nm) data produced by the Panoramic Camera (PanCam) instrument. We deployed a PanCam emulator at four hydrothermal sites in the Námafjall volcanic region of Iceland, a Mars-analogue hydrothermal alteration terrain. At these sites, sustained acidic–neutral aqueous interaction with basaltic substrates (crystalline and sedimentary) has produced phyllosilicate, ferric oxide, and sulfate-rich alteration soils, and secondary mineral deposits including gypsum veins and zeolite amygdales. PanCam emulator datasets from these sites were complemented with (i) NERC Airborne Research and Survey Facility aerial hyperspectral images of the study area; (ii) *in situ* reflectance spectroscopy (400–1000 nm) of PanCam spectral targets; (iii) laboratory X-ray Diffraction, and (iv) laboratory VNIR (350–2500 nm) spectroscopy of target samples to identify their bulk mineralogy and spectral properties. The mineral assemblages and palaeoenvironments characterised here are analogous to neutral–acidic alteration terrains on Mars, such as at Mawrth Vallis and Gusev Crater. Combined multispectral and High Resolution Camera datasets were found to be effective at capturing features of astrobiological importance, such as secondary gypsum and zeolite mineral veins, and phyllosilicate-rich substrates. Our field observations with the PanCam emulator also uncovered stray light problems which are most significant in the NIR wavelengths and investigations are being undertaken to ensure that the flight model PanCam cameras are not similarly affected.

1. Introduction

The European Space Agency/Roscosmos rover "ExoMars", scheduled for launch in 2018, has the primary objective of sampling the martian subsurface via a 2 m drill, and analysing the retrieved samples for geochemical and organic biosignatures (Vago et al., 2006). Key to this objective is the identification of geological and mineralogical surface deposits that are indicative of past habitable conditions. Such information is necessary to inform the selection of subsurface drill targets, samples of which will be scrutinised using a variety of contact and analytical instruments including a Raman Laser Spectrometer (RLS, Edwards et al., 2012), infra-red spectrometers (MicrOmega, Leroi et al., 2009; MA_MISS, Coradini et al., 2001), and a mass spectrometer (MOMA, Steininger et al., 2012). Regardless of whether or not there has been biological activity in martian history, the positive detection of astrobiologically interesting geological substrates proximal to the rover will be the first step in achieving this goal.

The scientific instrument providing the remote surface geological data for the ExoMars rover will be the Panoramic Camera (PanCam). This instrument comprises two Wide Angle Cameras (WACs), each with a 38.3° field of view (FoV), fixed 50 cm apart along an optical bench upon which a single High Resolution Camera (HRC) is also located (Coates et al., 2012). Each WAC is

* Corresponding author at: UCL/BBK Centre for Planetary Sciences, University College London, Gower Street, London WC1E 6BT, UK.
E-mail address: jennifer.harris@bbk.ac.uk (J.K. Harris).

http://dx.doi.org/10.1016/j.icarus.2015.02.004
0019-1035/

interfaced with a filter wheel containing 11 filters of predetermined wavelength, with all 22 filters dedicated to a particular scientific investigation (Table 1). Of these 22 filters, 6 are dedicated broadband red, green, and blue filters that will produce stereo colour composite images of the martian surface, while 12 filters are dedicated narrowband 'geology' filters that have been designed to capture and differentiate between the subtle spectral properties of phyllosilicates, sulfates, iron oxides, and major basaltic minerals within the limited Visible–Near Infrared (VNIR) wavelength range (440–1000 nm) captured by the PanCam Active Pixel Sensor (Cousins et al., 2010, 2012). Together with targeted monochrome and colour images provided by the HRC, WAC colour composite and multispectral data will be used for palaeoenvironmental interpretation of surface deposits and subsequent drill target selection. This is consistent with how similar camera suites on board the NASA Mars Exploration Rovers (MER) "Spirit" and "Opportunity" and Mars Science Laboratory (MSL) rover "Curiosity" have been successfully employed (Williams et al., 2013; Farrand et al., 2006, 2007, 2008, 2013, 2014). Additionally for ExoMars, targets within the WAC and/or HRC field of view can be further remotely scrutinised with the Infrared Spectrometer for ExoMars instrument (ISEM, spectral range 1.15–3.3 μm), which will also be mounted on the rover's mast (Korablev et al., 2013).

Over the past ten years, robotic exploration of Mars by the NASA MER missions, and recently NASA MSL Curiosity, has revealed a complex history of aqueous activity on Mars. Aqueous environments interpreted from these rover datasets range from acid sulfate leaching at Meridiani Planum (Squyres and Knoll, 2005), hydrothermal alteration of volcaniclastic deposits at Home Plate, Gusev Crater (Hurowitz et al., 2006; Morris et al., 2008; Schmidt et al., 2009), and aqueous, potentially hydrothermal alteration of basaltic impact breccias (Arvidson et al., 2014; Squyres et al., 2012). NASA's Mars Science Laboratory rover *Curiosity* has identified a range of lithologies influenced by aqueous activity, ranging from transported volcaniclastics (Schmidt et al., 2014), fluvial conglomerates (Williams et al., 2013), and the fine-grained sedimentary deposits at Yellowknife Bay comprising primary basaltic minerals and alteration phases. The latter includes amorphous material, smectite clays, and sulfates (Vaniman et al., 2014), potentially indicative of sustained hydrous environments (Grotzinger et al., 2014). Orbital data have similarly revealed an extensive array of aqueous alteration terrains (Murchie et al., 2009; Carter et al., 2013), including those formed via subsurface groundwater (Ehlmann et al., 2011), and sedimentary delta deposits where organic material may have a higher preservation potential (Ehlmann et al., 2008).

Table 1
Technical specifications of the current configuration of the ExoMars PanCam and the Aberystwyth University PanCam Emulator (AUPE-2). WAC filter bandpasses are given as Full Width at Half-Maximum (FWHM) values.

	AUPE-2 (updated from Pugh et al., 2012)	ExoMars Panoramic Camera
Wide Angle Cameras (WAC)		
Model	Manta G-504B	WAC
Image type	Mono (8–12 bit)	Mono (10 bit)
Sensor	Sony ICX655	Cypress STAR 1000 APS
Field of view	39° × 33°	38.3 × 38.3 ($h \times v$)°
Focal length	12 mm	21.85 mm
Image resolution	1024 × 1024	1024 × 1024
Aperture	*f*/11	*f*/10
Toe-In (cross over distance)	2.8° (5 m)	2.8° (5 m)
WAC filter wheels and their centre wavelengths and FWHM bandwidths[a,b]		
LWAC – geology 1	438 (24)	440 (25)
LWAC – geology 2	500 (24)	500 (20)
LWAC – geology 3	532 (10)	530 (15)
LWAC – geology 4	568 (10)	570 (12)
LWAC – geology 5	610 (10)	610 (10)
LWAC – geology 6	671 (10)	670 (12)
RWAC – geology 1	740 (13)	740 (15)
RWAC – geology 2	780 (10)	780 (20)
RWAC – geology 3	832 (37)	840 (25)
RWAC – geology 4	900 (50)	900 (30)
RWAC – geology 5	950 (50)	950 (50)
RWAC – geology 6	1000 (50)	1000 (50)
LWAC – blue broadband	440 (120)	440 (120)
LWAC – green broadband	540 (80)	540 (80)
LWAC – red broadband	640 (100)	640 (100)
RWAC – blue broadband	440 (120)	440 (120)
RWAC – green broadband	540 (80)	540 (80)
RWAC – red broadband	640 (100)	640 (100)
LWAC	545 (290) – visible	925 (5) – solar
LWAC	Empty – panchromatic	935 (5) – solar
RWAC	545 (290) – visible	450 (5) – solar
RWAC	Empty – panchromatic	670 (5) – solar
High Resolution Camera		
Model	Mantra G-146B	HRC
Image type	Mono (8–12 bit)	Mono (10 bit)
Sensor	Sony ICX267AL	Cypress STAR 1000 APS
Field of view	4.8°	4.8°
Focal length	58 mm	180 mm
Resolution	1024 × 1024	1024 × 1024
Aperture	*f*/11	*f*/14.4–20

[a] Final distribution and position of filters not yet determined. All filter centre wavelengths and bandpasses (in brackets) given in nm, with bandpasses at Full Width Half Maximum.
[b] Geology filter centre wavelengths and bandpasses from Cousins et al. (2012).

Ancient terrains (>3.5 Ga) in particular record a long history of aqueous activity and subsequent alteration (Ehlmann et al., 2011; Grindrod et al., 2012; Viviano et al., 2013). Noachian alteration mineral terrains have been found to include varying combinations of sulfates, phyllosilicates, zeolites, opaline silica, carbonates, and iron oxides (Murchie et al., 2009; Michalski et al., 2010; Viviano et al., 2013). Many of these have been attributed to hydrothermal alteration of basaltic substrates (Carter et al., 2013; Ehlmann et al., 2013). Low temperature hydrothermal environments such as these are a strong contender for isolated regions of habitability on early Mars (Schulze-Makuch et al., 2007; Cousins and Crawford, 2011; Ehlmann et al., 2011; Westall et al., 2013), potentially providing the necessary nutrients, metabolic redox couples, and liquid water needed for sustaining microbial populations, as terrestrial hydrothermal systems do on Earth. It is likely therefore that the ExoMars rover will encounter hydrated mineral terrains, and as such it is imperative that the rover's instruments are suitably prepared for this future deployment.

We sought to test the utility of ExoMars PanCam datasets in providing adequate information on the lithology and mineralogy of Mars-analogue terrains in Iceland formed by authigenic hydrothermal alteration of basalt with secondary mineral deposition. Iceland was selected as an ideal test site due to the occurrence of hydrated alteration assemblages similar to those on Mars (Ehlmann et al., 2012; Cousins et al., 2013). Specifically, we investigated the capability and limitations of WAC multispectral data in combination with WAC colour panoramas and monochrome HRC mosaics, in accurately representing the diverse alteration mineral assemblages and lithologies present at metre to sub-metre scales. Previous field-tests of earlier generation flight-like PanCam prototypes in Svalbard, Norway, as part of the NASA/ESA Arctic Mars Analog Svalbard Expedition demonstrated the high scientific value of performing field tests within Mars analogue geological terrains (Amundsen et al., 2010; Schmitz et al., 2010; Barnes et al., 2011; Pugh et al., 2012). This has been further demonstrated with recent tests of MSL and ExoMars flight-like instruments on Antarctic Mars analogue samples (Bishop et al., 2013). For the first time we combine Mars analogue field test datasets from a flight-like ExoMars PanCam instrument with *in-situ* (400–1000 nm), laboratory (350–2500 nm), and aerial (500–2500 nm) analysis of visible–near infrared spectral properties, and bulk mineralogical composition by X-ray Diffraction. This field deployment also provides the first ground-truthed field-test of the updated geological filter wavelengths and bandwidths selected for the ExoMars PanCam (Cousins et al., 2012).

2. Geological setting

The Aberystwyth University PanCam Emulator-2 (AUPE-2, Pugh et al., 2012) was deployed at sites around the Námafjall geothermal region in northeast Iceland. The Námafjall and nearby Krafla central volcanic system forms a graben within an active rifting zone, characterised by basaltic subaerial lava flows and subglacially-erupted volcaniclastic deposits and pillow basalts, with Mt. Námafjall itself comprising of a glaciovolcanic hyaloclastite ridge (Gudmundsson et al., 2010). The ridge and the subaerial basaltic lavas to the east have been subject to volcanogenic hydrothermal alteration producing localised patches of diverse alteration mineral assemblages among regions of unaltered primary basalt (Fig. 1). The water source for geothermal fluids in this area is thought to derive from high-elevation precipitation, likely within the Vatnajökull (glacier) area (Ármannsson, 2005; Gudmundsson et al., 2010). The active geothermal environments in the area are

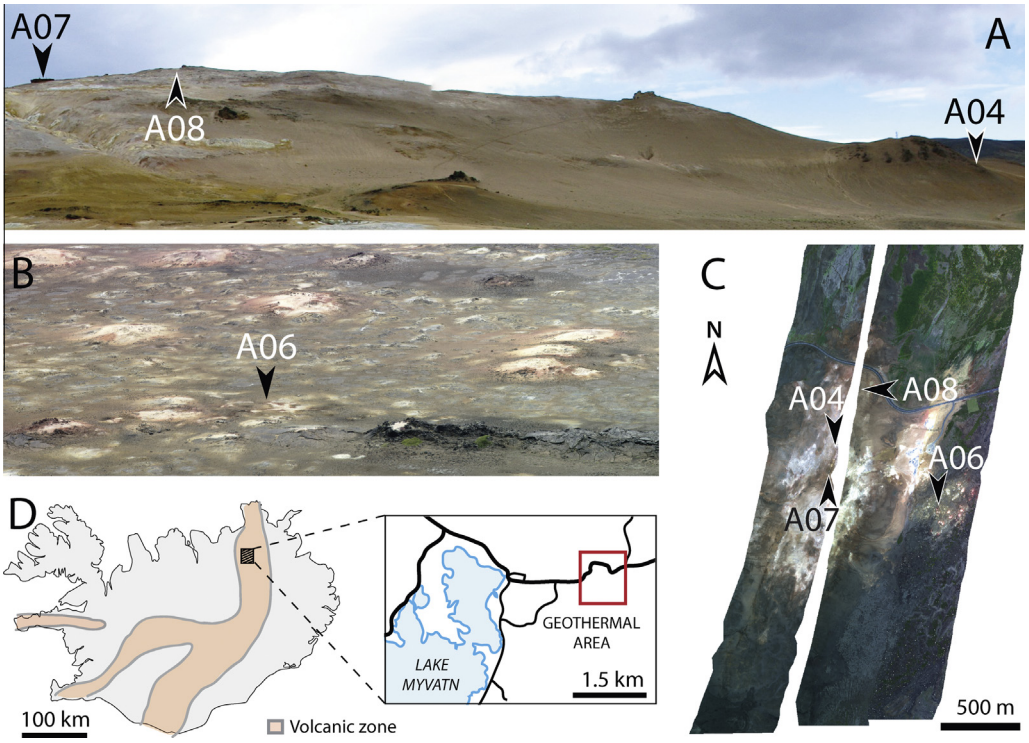

Fig. 1. Localities used for field-testing the ExoMars PanCam emulator "AUPE-2". (A) Volcaniclastic ridge where sites A04_Tuff, A07_Pillow, and A08_Vein are located, as viewed from site A06_Soils; (B) altered holocene subaerial basaltic lava flows where site A06_Soils is located (as viewed from the summit of the ridge in (A); (C) colour composite sections of ARSF Eagle swath data with all 4 sites shown; (D) map of Iceland showing the location of Námafjall within the northern volcanic zone – map inset shows the location of the Námafjall geothermal area. (For interpretation of the references to colour in this figure legend, the reader is referred to the web version of this article.)

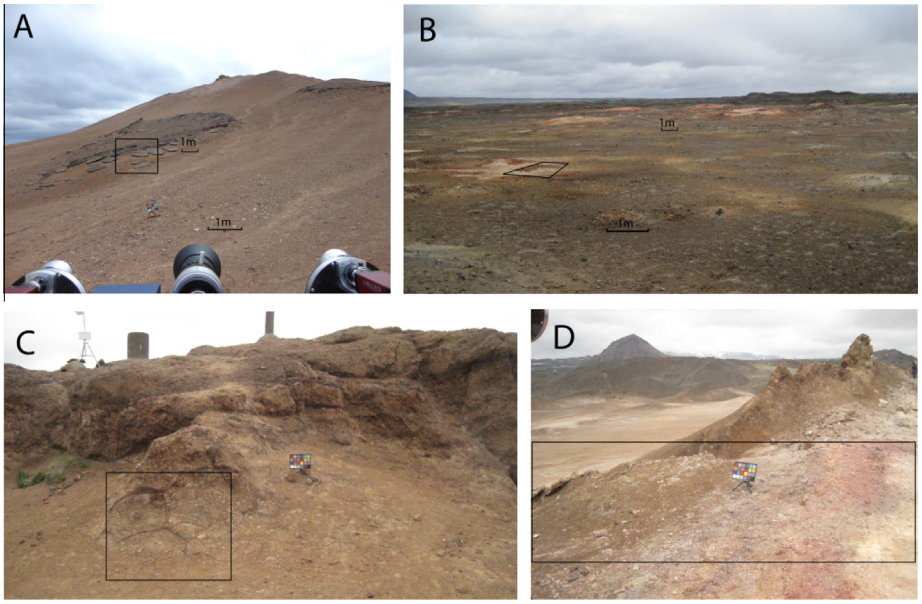

Fig. 2. Field photographs showing target sites. (A) A04_Tuff with similar structure in the top right. (B) A06_Soils (box, middle left) with surrounding similar soils and low mounds. (C) A07_Pillow, the calibration target in this photo is not in the same position as Fig. 7, that region of the image is the front section of the pillow formation. (D) A08_Vein showing exposed nature of target. Black boxes indicate approximately the regions imaged by AUPE-2 in Figs. 5 (2A), 6 (2B), 7 (2C) and 8 (2D).

colonised by a range of microbial populations, many of which derive their energy through chemolithotrophic metabolism (Huber and Stetter, 1991), indicating the present-day habitability of active sites. Four locations were selected for PanCam testing around Námafjall (Figs. 1 and 2). Three are located along the volcaniclastic ridge: (i) A04_Tuff (65°38′42″N, 16°49′01″W), a hydrovolcanic layered tuff; (ii) A07_Pillow (65°38′24″N, 16°49′15″W), a heavily-altered outcrop of subglacially-erupted pillow basalts; and (iii) A08_Vein (65°38′27″N, 16°49′13″W), a series of mineral veins cross-cutting the surrounding unconsolidated geothermal substrate. The fourth site, (iv) A06_Soils (65°38′15″N, 16°48′21″W) lies within a low-lying inactive zone of hydrothermal alteration, and comprises of a patch of semi-consolidated soils bearing a number of different visible alteration phases.

3. Methodology

3.1. Aerial hyperspectral data

Aerial datasets of the Námafjall region were acquired from the archived dataset IPY07-09 from the NERC Airborne Research and Survey Facility (ARSF), courtesy of the NERC Earth Observation Data Centre. The dataset was collected on 05/09/2008 from an altitude of approximately 1410 m using the two hyperspectral instruments operated by ARSF at the time of data collection: an AISA Eagle and an AISA Hawk. The Eagle is a VNIR hyperspectral sensor capable of collecting data spanning 400–970 nm at a maximum spectral resolution of 2.9 nm in a 1000 pixel swath. The Hawk covers 970–2450 nm at a maximum spectral resolution of 8 nm and a swath width of 320 pixels. The hyperspectral data were supplied as L1b data (non-georectified 'radiance at sensor'). The hyperspectral data was atmospherically corrected using the FLAASH module in Exelis Visual Information Solutions ENVI 4.8 (Exelis Visual Information Solutions, Boulder, Colorado) to generate ground surface reflectance values. These atmospherically-corrected datasets were then georeferenced to L3a level data using ARSF supplied software 'azgcorr' (Azimuth Systems UK, version 5.0.0, July 2005) and the supplied LiDAR DEM to a 2 m pixel resolution. The LiDAR operated by the ARSF at this time was an Optech Airborne Laser Terrain Mapper 3033. The LiDAR data was supplied as a final data product DEM supplemented with ASTER DEM data to fill any data gaps. Regions of significant atmospheric H_2O were removed from the final datasets leaving a total of 232 spectral bands. Reflectance spectra (0.5–2.5 μm) extracted from ground targets were extracted as 12 pixel means. These final datasets were used to guide our selection of ground targets through identification of regions of alteration and presence of hydrated minerals. Final selection of target sites was ultimately performed in the field.

3.2. Aberystwyth Panoramic Camera Emulator (AUPE-2)

AUPE-2 is a dedicated ExoMars PanCam emulator that has been constructed with commercial off-the-shelf cameras to replicate (as closely as possible) the data sets that will be acquired from the ExoMars PanCam. It comprises of two wide angle (39 × 33°) cameras (WACs) placed 50 cm apart along an optical bench, which in turn is fixed to a pan-tilt unit (Pugh et al., 2012). In front of each WAC is a filter wheel with 11 filter positions. Both filter wheels contain 3 broadband colour filters centred at 660 nm, 550 nm and 460 nm, a luminance filter covering the visible region of the spectrum and an empty filter slot for panchromatic imaging. Split evenly between the two WAC filter wheels and filling the remaining filter positions are 12 narrow band 'geology' filters spanning 440–1000 nm (see Table 1 for filter centre wavelengths and bandwidths). The filters are all hard coated interference filters comprised of thin film stacks on glass substrates. In addition to the WACs, a High Resolution Camera (HRC) with a field-of-view (FoV) ~ 5° is mounted in the centre of the optical bench, which provides close-up high resolution images of targets within the WAC FoV, consistent with the ExoMars PanCam (Coates et al., 2012). AUPE-2 was deployed *in-situ* at field localities, and a calibrated Macbeth ColorChecker© classic colour chart (X-rite) was included in one WAC image from each scene panorama to enable radiometric calibration of the AUPE-2 multispectral image data. All distances between AUPE-2 and outcrops are measured from the centre of the AUPE-2 optical bench to the centre of the calibration target. For all data acquisition, the AUPE-2 optical bench was positioned 2 m above the ground, consistent with the

ExoMars rover configuration. AUPE-2 data were collected between 10:30 and 14:40 local time under uniform grey skies, to minimise the atmospheric column the sunlight passed through and ensure consistent illumination during each dataset whilst eliminating the risk of specular reflections. The incidence and emission angles for each target region are highly dependent on local topography and vary within each scene. These conditions were largely dictated by the time and weather constraints inherent to fieldwork in Iceland but are also comparable to the use of MER Pancam on Mars (Farrand et al., 2007). ExoMars PanCam operations are still to be finalised but will be similar to those used in this work and by the MER Pancam team.

AUPE-2 multispectral data were processed using Exelis Visual Information Solutions ENVI 4.8 and IDL software (Exelis Visual Information Solutions, Boulder, Colorado) into relative reflectance calibrated image cubes following the calibration pipeline presented in Barnes et al. (2011), two cubes for each frame, one for each WAC. This pipeline encompassed flat-fielding, dark frame subtraction, removal of detector bias and the calculation of relative reflectance calibration factors from the in-scene Macbeth ColorChecker©. These final image cubes give R^* values, where R^* is defined by Reid et al. (1999) as "the brightness of the surface divided by the brightness of an RT (*Radiometric Calibration Target*) scaled to its equivalent Lambert reflectance." Region of Interest (ROI) spectra were extracted from these processed cubes using ENVI version 4.8. ROI footprints ranged in size from 20 (A04_Tuff), 40 (A06_Soils; A08_Vein) to 160 (A07_Pillow) pixels. Mean spectra were calculated over each ROI to be plotted with error bars representing the standard deviation over the pixels within each ROI. Footprint pixel sizes varied depending on the scale of variation in the scene and the distance of AUPE-2 from the target but all correspond to spatial footprints of approximately 1 cm radius. Principal Components Analysis (PCA) was performed on the ROI AUPE-2 spectra taken from the four sites ($n = 20$). Additionally PCA images were generating using the PCA tool resident in ENVI version 4.8 for each site.

3.3. In situ VNIR reflectance spectroscopy

Immediately following imaging of outcrop targets with AUPE-2, corresponding 400–1000 nm reflectance spectra of ROIs were acquired using an Ocean Optics Jaz portable spectrometer, using a Spectralon© calibration reference and an integrating sphere contact probe with an internal light source and a 10 mm diameter sample port. VNIR spectra were smoothed to remove noise inherent at the edge of the detector using a 3rd order polynomial Savitzky–Golay filter in Matlab (MATLAB Release 2012b, The MathWorks, Inc., Natick, Massachusetts, United States). AUPE-2 ROI R^* spectra were compared to their corresponding *in-situ* VNIR spectra, all of which were normalised to the 610 nm value (i.e. the spectral mid-point) to allow direct visual comparison of spectral morphology and accuracy of AUPE-2 R^* spectra. This normalisation reflects the *relative* nature of each dataset's reflectance values and does not imply an error in either dataset.

3.4. Laboratory VNIR spectroscopy and X-ray Diffraction

Rock and soil samples were retrieved immediately following a field spectrometer measurement from each ROI target for all outcrops imaged with AUPE-2. These were divided into two aliquots, one of which was powdered and sieved to <210 μm and the other left in its original consolidated state. The powdered samples were analysed using X-ray Diffraction to determine bulk mineralogical composition of ROI targets, while both the powdered and original samples were analysed using an ASD FieldSpec Pro spectrometer (spectral range 350–2500 nm) at the Natural Environment Research Council Field Spectroscopy Facility (NERC FSF) at the University of Edinburgh (www.fsf.nerc.ac.uk), using a contact probe attachment. XRD analysis was carried out as per previous studies (Cousins et al., 2012, 2013) using a Bruker D8 Advance XRD with a Vantec 1 detector at Aberystwyth University, calibrated using a corundum standard. For analysis of phyllosilicates, additional XRD analysis was conducted at Birkbeck, University of London using a Philips PW 1730 Diffractometer using Cu Kα radiation. The powdered samples for this analysis were prepared using standard methods described by Merriman and Peacor (1999) to ensure preferential orientation of the phyllosilicates. This preparation involved mixing the existing sieved powders with distilled water and centrifuging prior to removal of excess liquid. The resulting slurry was emplaced onto frosted glass slips and allowed to dry overnight prior to analysis. In both cases, sample spectra were compared to database mineral spectra using the International Centre for Diffraction Data database, and the RRUFF database (Downs, 2006).

3.5. Spectral parameters

Spectral parameters were utilised to emphasise features indicative of key minerals, bulk composition, or lithology (Table 2). Spectral parameters have proven to be an effective tool in the analysis of spectrally coarse data from the MER Pancam on both Spirit and Opportunity (Farrand et al., 2006, 2008, 2013; Rice et al., 2010, 2013). The spectral parameters used for this study have been adapted from those presented by Farrand et al. (2008) and Anderson and Bell (2013) for the geological filters on AUPE-2/ExoMars PanCam (Cousins et al., 2012).

4. Results

A summary of contextual mineralogical and spectral data for all site ROI units is given in Table 3. Broadly, alteration and secondary minerals identified in the ASD laboratory VNIR spectra (Fig. 3) include hematite, goethite, nontronite, montmorillonite, gypsum, and sulfur. Ferrihydrite, maghemite, and various zeolites also appear as minor constituents. Sample XRD analysis is consistent with the laboratory VNIR results, revealing alteration phases to include all the above, but also kaolinite, anatase, natrojarosite, trace calcite and quartz. Atmospheric H_2O obscures the mineral hydration regions in the ARSF aerial datasets; however a few mineral identifications were possible from within the atmospheric windows. Significant minerals included hematite, goethite, nontronite and other smectites. A vegetation signal was also prevalent across the scene, evidenced by a sharp increase in reflectance around 0.7 μm in a number of pixels in the aerial imagery (Fig. 4). AUPE-2 data for each of the four sites is described in the following sections.

4.1. Site A04_Tuff: hydrovolcanic outcrop

4.1.1. AUPE-2 data

This outcrop was imaged first from a distance of 7.75 m (Fig. 5A) as a 4×1 RGB panorama, followed by a single field of view (FoV) full multispectral image set from a distance of 3.3 m. The outcrop and similar nearby deposits are comprised of layered, semi-competent circular collapse features ranging in size from 5 to 15 m in diameter, surrounded by unconsolidated geothermal soils (Fig. 5A). The edges of these circular collapse features have weathered and fragmented along sedimentary bedding planes into slabs approximately 10 to 80 cm in size. Near-horizontal bedding planes, and individual slabs, are visible in the LWAC colour mosaic (Fig. 5B). This outcrop is less oxidised than the surrounding soils

Table 2
Spectral parameters calculated for AUPE-2 WAC multispectral data.

Name	Description	Rationale/related characteristic
BD532	Depth of absorption band centred at 532 nm $1-(R_{532}/[(0.53*R_{500})+(0.47*R_{568})])$	Identifies ferric minerals, in particular hematite and related to degree of oxidation
S532-610	Slope between 532 and 610 nm $(R_{610}-R_{532})/(610-532)$	Ferric minerals and dust
BD900	Depth of absorption band centred at 900 nm $1-(R_{900}/[(0.455*R_{840})+(0.545*R_{950})])$	Strength of NIR absorption, related to ferric minerals
S740-1000	Slope between 740 and 1000 nm $(R_{1000}-R_{740})/(1000-740)$	Strength and position of NIR absorption linked to ferrous minerals
S950-1000	Slope between 950 and 1000 nm $(R_{1000}-R_{950})/(1000-950)$	Linked to hydrated minerals
R740/1000	740:1000 nm ratio R_{740}/R_{1000}	Ferrous minerals
R671/438	671:438 nm (red:blue) ratio R_{671}/R_{438}	Ferric minerals and dust
BD610	Depth of absorption band centred at 610 nm $1-(R_{610}/[(0.600*R_{568})+(0.400*R_{671})])$	Can indicate goethite development and be influenced by olivine vs pyroxene
BD950	Depth of absorption band centred at 950 nm $1-(R_{950}/[(0.500*R_{900})+(0.500*R_{1000})])$	Related to hydrous minerals, some clays and silicates
S438-671	Slope between 438 and 671 nm $(R_{671}-R_{438})/(671-438)$	Related to degree of oxidation

Table 3
Summary of site ROIs, their mineralogy, and VNIR spectral features (also see Fig. 3).

	Unit	Bulk mineralogy (XRD, *VNIR*)	VNIR reflectance absorption features (μm)
A04_Tuff, 65°38′42″N, 16O49′01″W			
A04_001	Grey slab	Smectite, plagioclase, augite, kaolinite *Olivine, quartz*	0.48, 1.09 (broad), 1.41 (small), 1.92, 2.20, 2.29
A04_002	Alteration soil	Kaolinite, smectite, iron oxide, quartz, augite, plagioclase *Chabazite, montmorillonite, nontronite*	0.49, 0.65 (small), 0.96 (broad), 1.42, 1.91, 2.21, 2.29, 2.39
A04_003	Grey slab	Plagioclase, smectite, kaolinite, quartz *Olivine, quartz*	0.47, 0.65 (small), 1.07 (broad), 1.41, 1.92, 2.21, 2.30
A04_005	Alteration soil	Mordenite, alunite, nontronite, iron oxide *Nontronite, montmorillonite, ferrihydrite, goethite*	0.49, 0.65 (small), 0.963 (broad), 1.42, 1.91, 2.21, 2.29, 2.39
A06_Mound, 65°38′15″N, 16°48′21″W			
A06_001	Bright-toned unit	Sulfur, anatase *Nontronite, montmorillonite*	0.44, 0.97, 1.42, 1.77, 1.92, 2.22–2.26
A06_002	Bright-toned unit	Sulfur, zeolite *Sulfur*	0.40 (major), 0.92, 1.41, 1.91, 2.22
A06_003	Dark red unit	Hematite, natrojarosite, augite, sulfur (trace) *Hematite*	0.53, 0.90, 1.41, 1.47, 1.91, 2.21, 2.27
A06_004	Bright-toned unit	Sulfur, zeolite *Sulfur*	0.40 (major), 0.96 (broad), 1.42, 1.91, 2.22
A06_005	Dark red unit	Natrojarosite, sulfur, zeolite *Goethite, montmorillonite*	0.49, 0.93, 1.42, 1.47 (tiny), 1.91, 2.22, 2.27, 2.47
A06_006	Bright-toned unit	Sulfur *Nontronite, montmorillonite*	0.44, 0.48, 0.91, 1.16 (tiny), 1.41, 1.77, 1.91, 2.22, 2.26, 2.47
A07_Pillow, 65°38′24″N, 16°49′15″W			
A07_001	High albedo nodule	Calcite, plagioclase, mordenite *Zeolite*	1.05, 1.42, 1.92, 2.21, 2.30, 2.40
A07_002	Dark quench rind	Smectite, calcite, stilbite *Nontronite, chabazite*	0.49, 0.99, 1.43, 1.78, 1.92, 2.29, 2.40
A07_003	Pillow core interior	Plagioclase, smectite, stilbite, iron oxide *Nontronite*	0.42, 0.48 (minor), 0.65 (minor), 1.02, 1.42, 1.92, 2.19, 2.30, 2.39
A07_004	Pillow core interior	Plagioclase, smectite, stilbite, kaolinite *Nontronite*	0.42, 0.48, 0.60 (shoulder, minor), 1.03, 1.42, 1.78 (minor), 1.92, 2.20, 2.30, 2.40
A08_Veins, 65°38′27″N, 16°49′13″W			
A08_001	Dark red unit (mineral vein)	Gypsum *Gypsum*	0.42, 0.49, 1.19, 1.45, 1.49, 1.54, 1.75, 1.95, 2.22, 2.27, 2.42
A08_002	Dark red unit	Plagioclase, smectite, zeolite, iron oxide, opal-a *Goethite, nontronite*	0.49, 1.01, 1.43, 1.92, 2.21, 2.29, 2.40
A08_003	Brown soil	Hematite, gypsum, smectite *Hematite, gypsum*	0.54, 0.89, 1.45, 1.49, 1.54 (both minor), 1.75, 1.94, 2.21, 2.27, 2.43
A08_004	Brown soil	Hematite, alunite, gypsum, smectite, zeolite *Hematite, gypsum*	0.53, 0.90, 1.44, 1.77, 1.93, 2.21, 2.46
A08_005	Brown soil	Gypsum, hematite, smectite, zeolite *Gypsum, goethite*	0.52, 0.65, 0.91, 1.45, 1.49, 1.54, 1.75, 1.94, 2.21, 2.27, 2.43
A08_006	Peach soil	Gypsum, zeolite, smectite, hematite *Gypsum, montmorillonite*	

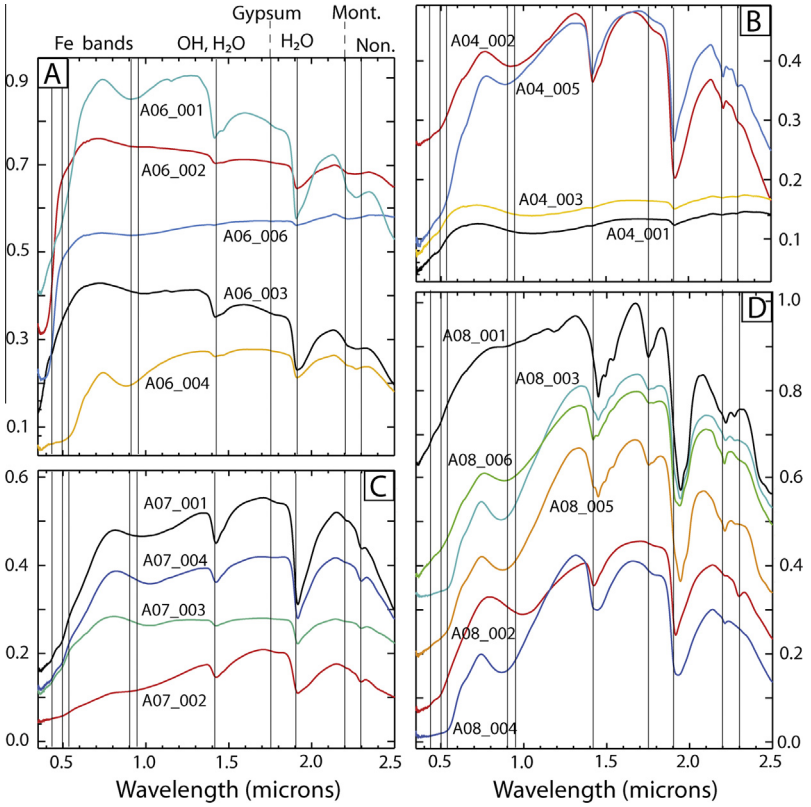

Fig. 3. Laboratory ASD VNIR reflectance spectra of AUPE-2 ROI target samples. Individual sample names follow the format 'Site#_ROI#'. Absorption lines are shown for Fe crystal field bands, vibrational bands relating to H_2O and OH, and key absorption bands for gypsum, montmorillonite (mont.) and nontronite (non.).

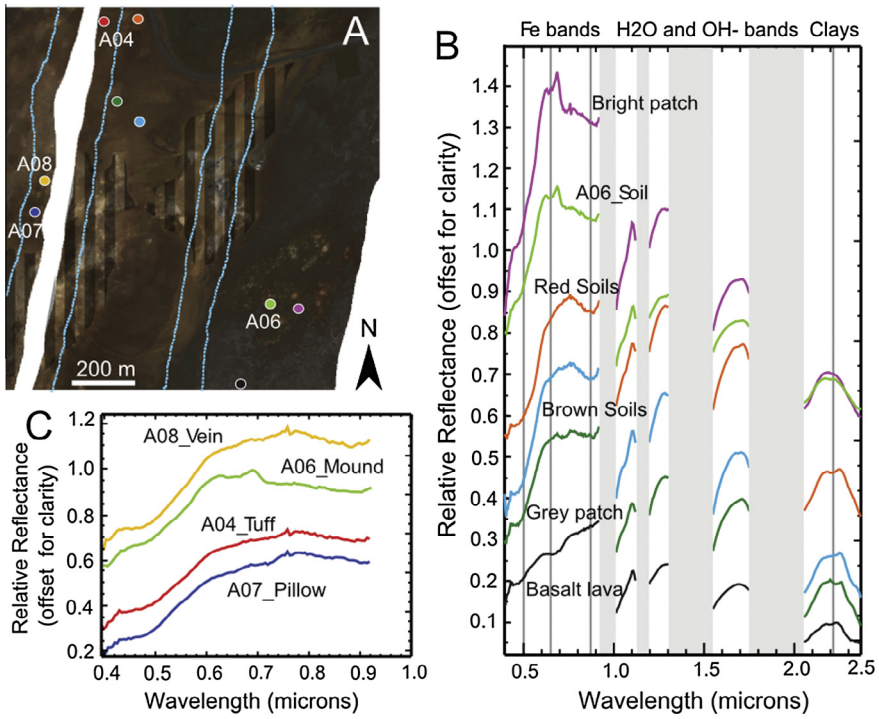

Fig. 4. ARSF aerial spectral analysis. (A) Eagle RGB composite (bands 61, 39, 20) showing locations of spectra in (B and C) (spot-size not representative of sampling footprint), and approximate areas of ongoing hydrothermal activity (striped regions), which were excluded from site selection. Blue dashed lines indicate edges of Hawk swaths; (B) 0.4–2.5 μm relative reflectance spectra (each off-set by 0.1 for clarity) from soil targets across the test site; (C) 0.4–0.9 μm reflectance spectra from all four sites. (For interpretation of the references to colour in this figure legend, the reader is referred to the web version of this article.)

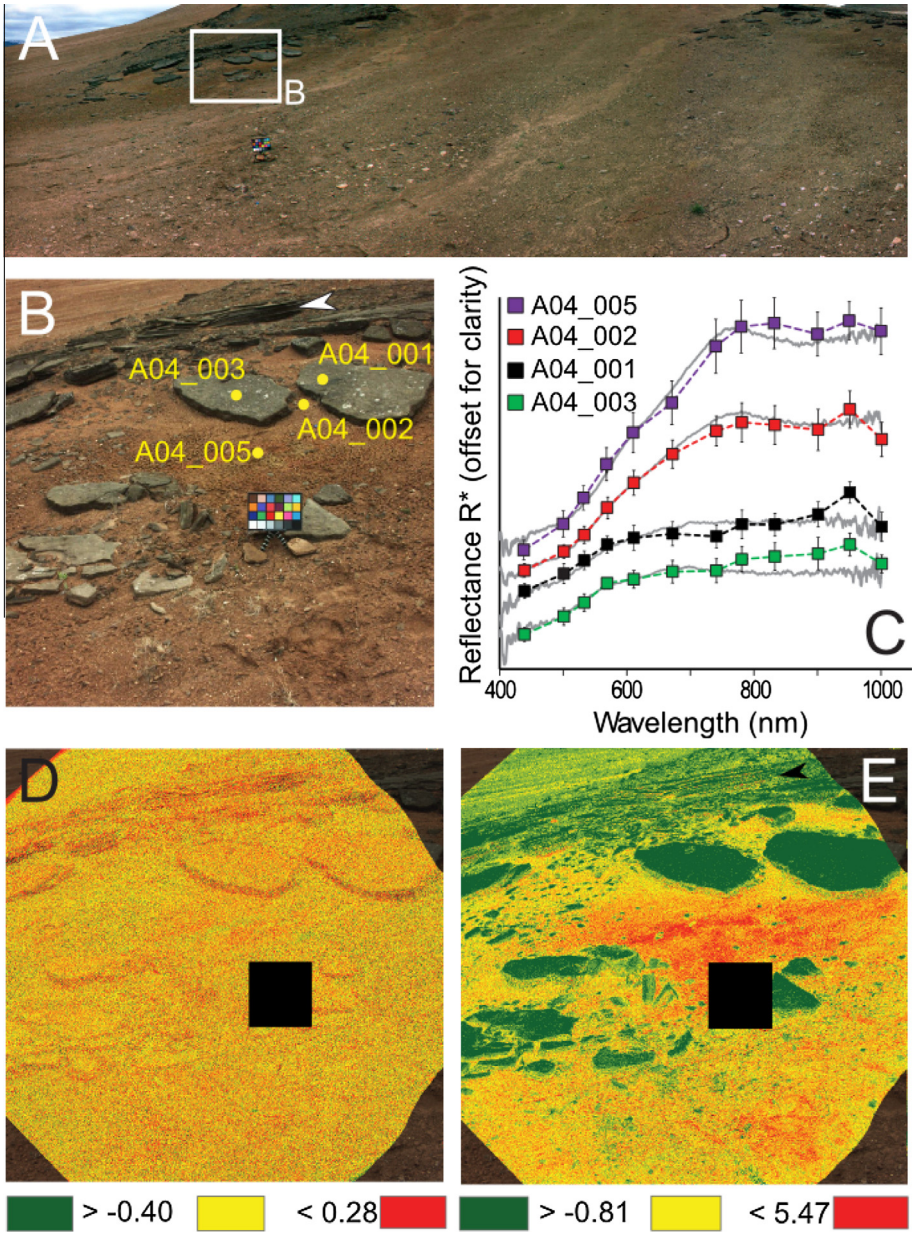

Fig. 5. AUPE-2 datasets for site A04_Tuff. (A) LWAC colour panorama of the outcrop (top left) and the surrounding area, with the 21.5 × 28 cm ColorChecker© for scale; (B) single LWAC FoV colour image showing location of AUPE-2 ROI targets (footprints not to scale), and arrow highlighting sedimentary bedding; (C) AUPE-2 R^* spectra and corresponding *in-situ* field spectra (grey); (D) LWAC spectral parameter image of the 610 nm band depth (BD610); (E) LWAC spectral parameter image of the narrowband red:blue ratio (R671/438). Black boxes in (D and E) indicate the location of the ColorChecker©. (For interpretation of the references to colour in this figure legend, the reader is referred to the web version of this article.)

(Fig. 5B), exhibiting a low-albedo, spectrally flat reflectance profile (ROIs A04_001 and A04_003, Fig. 5C) consistent with the grey surface colour of this lithology. This differentiation is clearly emphasised in the narrowband red:blue ratio (R671/438) spectral parameter image (Fig. 5E), highlighting the steeper ferric absorption slope of the soils. Spectrally, the site forms three distinct units (Fig. 5C and E): the sedimentary grey slab unit (ROI's A04_001 and A04_003), and two alteration soil units (A04_002 and A04_005) surrounding the grey slab unit. Despite the homogenous visible colour of the alteration soils (Fig. 5B), they show a clear variation in the ratio between red and blue (R671/438), highlighting those regions with a higher proportion of ferric minerals. In addition, the R671/438 spectral parameter image further reveals the sedimentary layering in the grey slab unit, even in areas where the colour image shows only shadow (Fig. 5E).

AUPE-2 R^* spectra measured from ROIs A04_001 and A04_003 within the grey slab unit show a consistent match in spectral profile to the *in situ* reflectance spectrometer data (Fig. 5C). The only deviation in reflectivity is seen at the 950 nm band, with the AUPE-2 R^* spectra showing a sharp increase in reflectance at this wavelength. Overall, the grey slab unit spectra have a low albedo, and are flat and featureless in this wavelength range. Conversely, ROIs A04_002 and A04_005 from the surrounding alteration soils both show an Fe^{3+} absorption in the NIR in both R^* and *in-situ* reflectance spectra, suggesting the presence of iron-oxide mineral species or nanophase material. These NIR absorptions in the R^* spectra are not as broad as the *in-situ* reflectance measurements, beginning at the 832 nm filter rather than at 780 nm in the *in-situ* spectra. The R^* spectrum for ROI A04_005 also captures the red shoulder seen in the *in-situ* spectrum at 640 nm, although due to

the difference in spectral resolution it is captured at the 671 nm filter. Again the R^* spectrum displays a negative slope between 950 nm and 1000 nm that is not seen in the corresponding reflectance spectral data.

4.1.2. Contextual mineralogy and field observations

The grey slab unit is characterised by finely-layered volcaniclastic sediments comprising of unaltered basaltic glass (siderome-lane) clasts (<2–3 mm grain size) supported by a fine-grained amorphous grey-beige matrix, typical of volcanic sediments emplaced via hydrovolcanism. Clasts are angular and largely unsorted, suggesting deposition proximal to the source, though in some parts of the outcrop clasts form semi-defined bands of coarser and finer material, along which bedding planes form. The fine-grained matrix itself is in the early stages of palagonitisation (Stroncik and Schmincke, 2002), and has undergone little oxidation. The circular constructs are not discernible within the aerial data, but lie within the bright-toned region of alteration along Námafjall ridge (Fig. 1C). Aerial spectral data from this region show broad absorption features at 0.5 and 0.9 μm suggesting the presence of iron-oxide minerals and subtle absorptions at 2.2 and 2.3 μm indicative of smectite clays or opaline silica (Fig. 4). Laboratory VNIR (350–2500 nm) spectra (Fig. 3) of grey slab unit ROIs A04_001 and A04_003 exhibit few absorption features in the 0.4–2.5 μm range, dominated only by a broad Fe^{2+} absorption centred around 1.0 μm and a minor H_2O band at 1.9 μm. Surrounding soil target ROIs A04_002 and A04_005 both show a broad Fe^{3+} absorption at 0.9 μm (consistent with the NIR absorption observed in the R^* and *in situ* reflectance data) with well-defined OH^- and H_2O absorptions at 1.4 and 1.9 μm respectively, together with minor absorptions at 2.2 and 2.3 μm, indicative of smectite clay minerals montmorillonite and nontronite (Bishop et al., 2008). XRD analysis is consistent with the results, showing the grey slab units to be predominantly plagioclase and smectite and the soils to be smectite and unidentified iron oxides.

4.2. Site A06_Soils: extinct fumarole patch

4.2.1. AUPE-2 data

This target was imaged from a distance of 1.56 m in a 2 × 1 panorama. The LWAC colour mosaic (Fig. 6A) of this target reveals a multitude of heterogeneous, loosely-consolidated soils, which broadly form a bright-toned grey–pink unit and a low-albedo dark-red unit. These are emphasised by the narrowband red:blue ratio (R671/438) spectral parameter image (Fig. 6D). Structurally, this region appears to be comprised of one poorly consolidated unit, with no observable internal structural units. The WAC PCA image (Fig. 6B) and the green–red slope (S532-610) spectral parameter image (Fig. 6E) show spectral variation is intimately mixed throughout the bright-toned unit implying a well-mixed soil composition on the sub-metre scale. Six ROI targets were selected within this outcrop, and were chosen based on visible colour variations identified within the LWAC colour mosaic. ROI A06_001 lies within the high albedo bright-toned unit, and exhibits

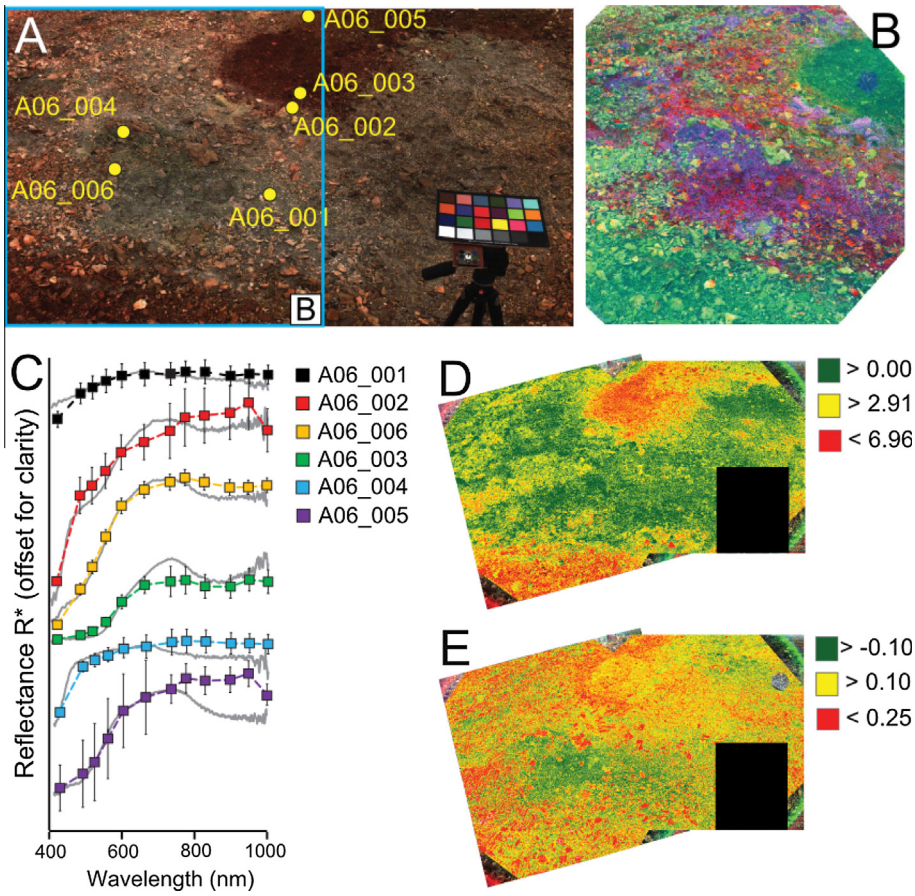

Fig. 6. AUPE-2 datasets for site A06_Soils. (A) LWAC colour panorama with the 21.5 × 28 cm ColorChecker© for scale, showing location of ROI targets (footprints not to scale) and region covered in (B); (B) LWAC principal component image (R = PC1, G = PC3, B = PC4) where red highlights white-coloured minerals, green highlights iron oxide-rich soils, and purple highlights sulfur; (C) AUPE-2 R^* spectra and corresponding field reflectance spectra (grey); (D) LWAC spectral parameter image of narrowband red:blue ratio (R671/438), (E) slope between 532 and 610 nm (S532_610). Black boxes in (D and E) indicate the location of the ColorChecker©. (For interpretation of the references to colour in this figure legend, the reader is referred to the web version of this article.)

a flat spectrum with no absorption features (Fig. 6C), potentially indicative of alteration minerals such as gypsum, opaline silica, zeolites, or magnesium sulfate (Hunt and Ashley, 1979; Cloutis et al., 2002; Ehlmann et al., 2012). The AUPE-2 R^* spectra for this ROI accurately captured this spectral profile at all wavelengths as identified with the corresponding spectrometer field measurement except for the 440 nm value. The slightly steeper slope at this position is likely a result of a slight spatial mismatch between the measurements and the high variability of this target resulting in the AUPE measurement including slightly more sulfur than the *in-situ* measurement. ROI A06_004 exhibits a sharp slope in the blue followed by a broadly flat spectrum through the visible and NIR. This spectral shape is characteristic of sulfur, and like ROI A06_001, it is accurately captured by the AUPE-2 R^* spectrum (Fig. 6C). The ROI A06_005 spectrum from the low albedo dark-red unit displays features consisted with ferric iron-bearing minerals, and in the visible the AUPE-2 data captures the absorption at 510 nm followed by the shoulder at 600 nm (Fig. 6C), but fails to capture the deep, broad absorption that characterises the NIR, centred at 950 nm. Similarly, the R^* spectrum for ROI A06_003 is consistent with the corresponding *in-situ* measured spectrum in the visible, but fails to capture the reflectance peak at 740 nm despite the presence of filters within this region.

4.2.2. Contextual mineralogy and field observations

While the particular outcrop imaged by AUPE-2 at this site is not resolvable in detail in the aerial data due to its small spatial extent, it is within a cluster of bright-toned, high albedo alteration patches that are clearly distinct from the surrounding unaltered basaltic terrain (Fig. 1C). These high albedo patches all have similar spectra in the ARSF aerial dataset (Fig. 4), showing absorptions around 0.47, 0.66 and 0.9 μm, indicating that ferric minerals are present. This implies that the soils imaged by AUPE-2 may be representative of the other discrete alteration patches within this cluster. Within the target itself, the low-albedo dark red unit (ROIs A06_003, A06_005) is comprised of a heterogenous mix of hematite, goethite, montmorillonite, natrojarosite, jarosite, augite, sulfur, and opaline silica as determined by laboratory reflectance spectra (Fig. 3) and XRD data (Table 3). The bright-toned unit ROIs have a less-varied mineralogy. ROIs A06_001 and A06_006 both comprise of smectite clays and sulfur, while ROIs A06_002 and A06_004 are dominated solely by sulfur. The target is interpreted to be an extinct acid fumarole patch consistent with the nearby active geothermal area, with the sulfur-rich soils representing the high-temperature parts of the fumarole.

4.3. Site A07_Pillow: pillow basalts

4.3.1. AUPE-2 data

The context LWAC colour image, taken from a distance of 2.1 m, captures the distinctive morphology and cross-sectional structure of a pillow basalt sequence (Fig. 7A). The outcrop surface is extensively weathered and altered, with the dark quench rinds of the individual pillows contrasting with the oxidised crystalline pillow core. In the PCA LWAC image (Fig. 7C) these quench rinds stand out as bright green structures, with the more oxidised base of the outcrop displayed in purple. Sub-cm sized cross-cutting mineral veins and larger nodules are strongly visible in yellow, and their emplacement does not appear to have been influenced by the existing pillow basalt structures. The HRC image (Fig. 7E) confirms

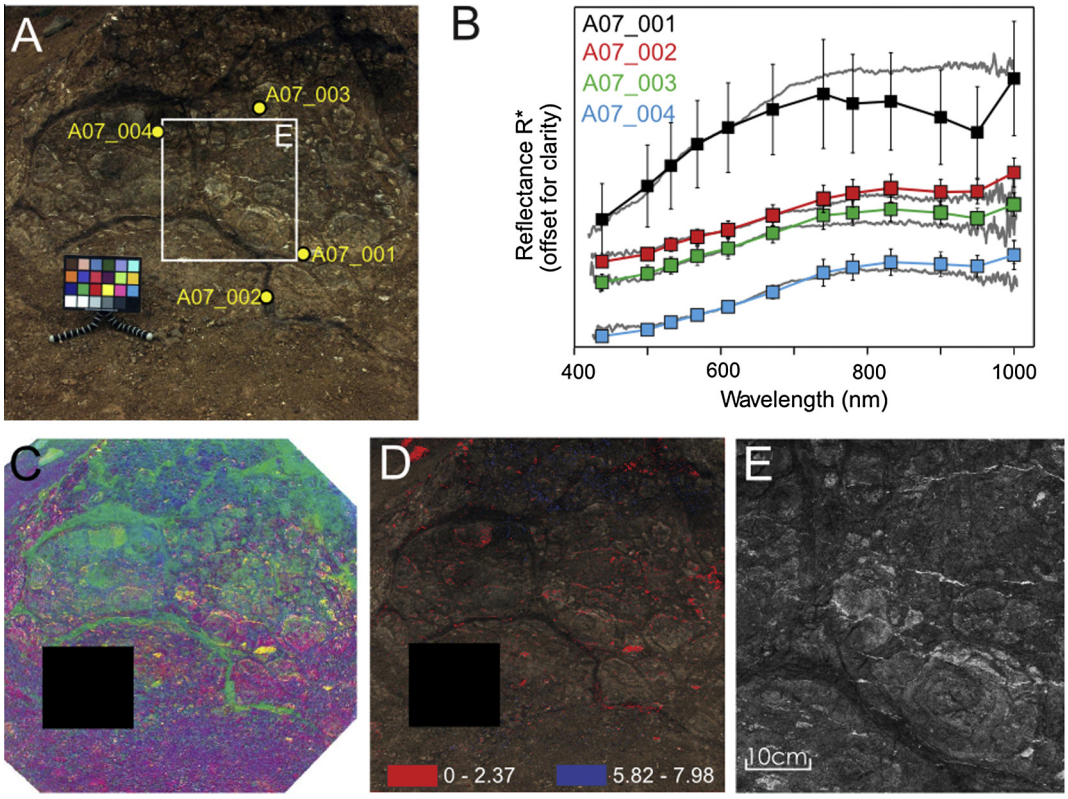

Fig. 7. AUPE-2 datasets for site A07_Pillow. (A) LWAC colour image of the outcrop face (21.5 × 28 cm ColorChecker© for scale), showing ROI targets (footprint not to scale) and HRC footprint E; (B) AUPE-2 R^* spectra and corresponding field spectra (grey); (C) PCA image (R = PC1, G = PC2, B = PC3) highlighting glass-rich quench rinds (green) and zeolite veins and nodules (yellow); (D) LWAC spectral parameter image of the narrowband red:blue ratio (R671/438) showing the distribution of fine mineral veins throughout the outcrop; (E) HRC image of the altered pillow cross-sections and cross-cutting zeolite mineral veins. Black boxes in (D and E) indicate the location of the ColorChecker©. (For interpretation of the references to colour in this figure legend, the reader is referred to the web version of this article.)

the presence of the high albedo mineral veins observed in the LWAC image. These high albedo veins are also picked out as red in the narrowband red:blue ratio (R671/438) spectral parameter image (Fig. 7D), showing their distribution across the whole outcrop and not just within the footprint of the HRC target. Concentric weathering rinds are well-formed across the surface of the outcrop, and are visible in the context WAC colour and greyscale HRC images (Fig. 7A and E).

Spectrally, ROI A07_001 from the high-albedo nodule shows the highest reflectance and the steepest visible slope (Fig. 7B) in the *in-situ* reflectance spectra. The emplacement of this deposit as secondary mineral veins, together with its high albedo and featureless spectral profile, suggests these veins likely comprise of either low temperature phases such as gypsum, zeolite, calcite or opaline silica, or higher temperature phases such as quartz. It is not possible to distinguish between these minerals from AUPE-2 multispectral data, due to the lack of absorption features within the PanCam spectral range of 440–1000 nm for these minerals. The R^* spectral profile of this ROI agrees with the *in-situ* reflectance spectra for the visible wavelengths only. The near-infrared (NIR) part of the R^* spectrum shows a deep skewed absorption from 832 nm to 1000 nm centred at 950 nm, which is inconsistent with the *in-situ* reflectance spectrum (Fig. 7B). The other three ROI's are measured from the pillow core interior unit (A07_003 and 004) and dark quench rind (A07_002). These are all low albedo, with a slight positive slope in the visible portion of the R^* spectra and slight negative slopes in the NIR (Fig. 7). These three are consistent (within error bars) with the corresponding *in situ* spectrometer data up to 950 nm. The slight positive slope in these three AUPE-2 R^* spectra from 950 to 1000 nm are not supported by the *in situ* reflectance spectra. A discrepancy at these bands is prevalent throughout the AUPE-2 dataset and is discussed more fully in Section 4.6.2.

4.3.2. Contextual mineralogy and field observations

As with the outcrops imaged at site A04_Tuff, the pillow basalt outcrop was not identifiable from the ARSF aerial data, and lies within an area of pale-brown alteration (Fig. 1C). The aerial data only covers this site in the Eagle swath and shows the general shape of an iron bearing mineral rock or soil with broad absorption features at 0.48 and 0.9 μm (Fig. 4). Bulk mineralogy of ROI samples determined through XRD analysis and VNIR laboratory spectra shows the altered surface of the pillow basalt outcrop to comprise of nontronite, goethite, and ferrihydrite. Basalt vesicles are infilled with zeolite amygdales, presumably originating from the same hydrothermal fluids that precipitated the mineral veins. These amygdales are not identifiable in the WAC or HRC datasets due to their small size (<3 mm), despite their prevalence throughout the outcrop. The zeolites do however influence the laboratory reflectance spectra measured from the powdered and homogenised ROI subsamples, producing OH^- and H_2O absorptions at 1.4 and 1.9 μm, increasing overall albedo, and producing a weak Fe^{2+} absorption at 490 nm in all samples (Fig. 3).

4.4. Site A08_Veins: gypsum veins

4.4.1. AUPE-2

A 3 × 1 LWAC panorama was acquired at this site, from a distance of 2.90 m. The region comprises exposed mineral veins surrounded by unconsolidated alteration soils (Fig. 8). From the LWAC colour panorama, three distinct units can be identified: a structured dark red unit intercalated with higher-albedo linear ridges, a brown soil unit, and finally bright-toned alteration soils (Fig. 8A). The equivalent red:blue ratio (R671/438) spectral parameter image (Fig. 8C) highlights the spectral variety present across the whole scene. The high albedo mineral vein ridges visible within the dark red unit are positioned prominently above the surrounding unconsolidated dark-red soils. Conversely the bright-toned alteration soils to the right of the image form a distinctive 'stripe', but no structural prominence. AUPE-2 R^* spectra taken from the structured dark red and brown soil units agree well in the visible with the corresponding *in-situ* reflectance spectra (Fig. 8B), but the infrared portion shows disagreement beyond 740 nm. *In-situ*

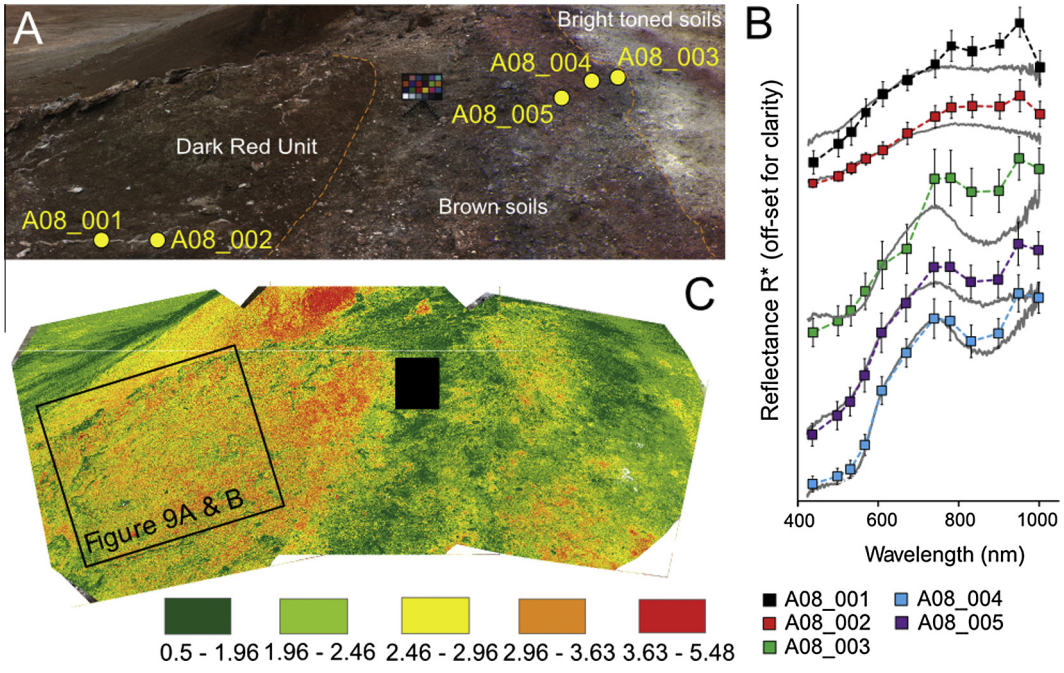

Fig. 8. AUPE-2 datasets for site A08_Vein. (A) LWAC colour panorama (21.5 × 28 cm ColorChecker© for scale) showing spectral units and ROI targets (footprints not to scale); (B) AUPE-2 R^* spectra of the two main spectral units and corresponding field spectra (grey); (C) LWAC spectral parameter panorama of the narrowband red:blue ratio (R671/438), box inset shows footprint of Fig. 9A and B. The black box in (C) indicates the location of the ColorChecker©. (For interpretation of the references to colour in this figure legend, the reader is referred to the web version of this article.)

reflectance spectra from ROI's A08_003 to 005 within the brown soil unit all show similar features including a slope increase between 530 and 550 nm, and a very broad absorption centred at 870 nm. These features are captured by the AUPE-2 multispectral data. ROIs A08_001 and A08_002 from the high albedo mineral vein ridges and surrounding soil respectively have a featureless *in-situ* reflectance spectra, with a long shallow positive slope in the visible levelling out to a flat slope in the infrared (Fig. 8B). The corresponding R^* spectra show a steeper visible slope for A08_001 and an absorption centred at 832 nm followed by a steeply negative slope from 950 to 1000 nm. This last feature is again unique to the R^* spectra. AUPE-2 R^* A08_001 and A08_003 also both deviate from the *in-situ* spectral measurements in the visible at 440 nm outside of the error bars. Both measurements however, do match the laboratory spectra suggesting that the *in-situ* measurements have been contaminated by dust in the field. False colour (Fig. 9A) and spectral parameter (Fig. 9B) images highlight the bright-toned mineral veins within the dark red unit, showing them to be spectrally distinct from the surrounding soils and forming long, structurally-competent deposits. HRC mosaics (Fig. 9C and D) of these features reveal the undulating morphology of these veins. Surface weathering can be seen on the exposed surfaces of the mineral veins, which has resulted in semi-rounded fragments of the deposit lying at the base of the vein (Fig. 9D). Loose fragments such as this one are also clearly picked out in the false colour image (Fig. 9A).

4.4.2. Contextual mineralogy

Unlike the high-albedo cross-cutting mineral veins in the pillow basalt outcrop (A07_Pillow), these larger, more prominent veins are comprised of gypsum, as confirmed by both the laboratory VNIR spectroscopy and the XRD results. The surrounding unconsolidated altered soils are broadly similar in mineralogical composition to the soils at site A04_Tuff, being characterised by smectite clays and iron oxides (montmorillonite and goethite at A04_Tuff; montmorillonite and hematite at A08_Vein). The exception to this is that the soils at this site also contain gypsum, most likely weathered out from the surrounding veins. The prominent ridges produced by the mineral veins are too small to be resolved within the aerial image, but lie within the distinct zone of alteration characterised by high albedo deposits. This site lies outside the swath of the ARSF Hawk aerial instrument but within that of the Eagle instrument. The resulting spectrum extracted from the surrounding area (Fig. 4) shows broad absorptions at 0.48 and 0.88 μm indicating the presence of iron bearing minerals such as goethite and hematite.

4.5. Principal Component Analysis

The vast majority (99%) of the variance for all sites was contained within the first 3 principal components (91.19%, 5.88% and 1.74% respectively). The R^* spectra PCA results (Fig. 10) show tight clusters of A04_Tuff ROIs from the grey slab unit and A07_Pillow

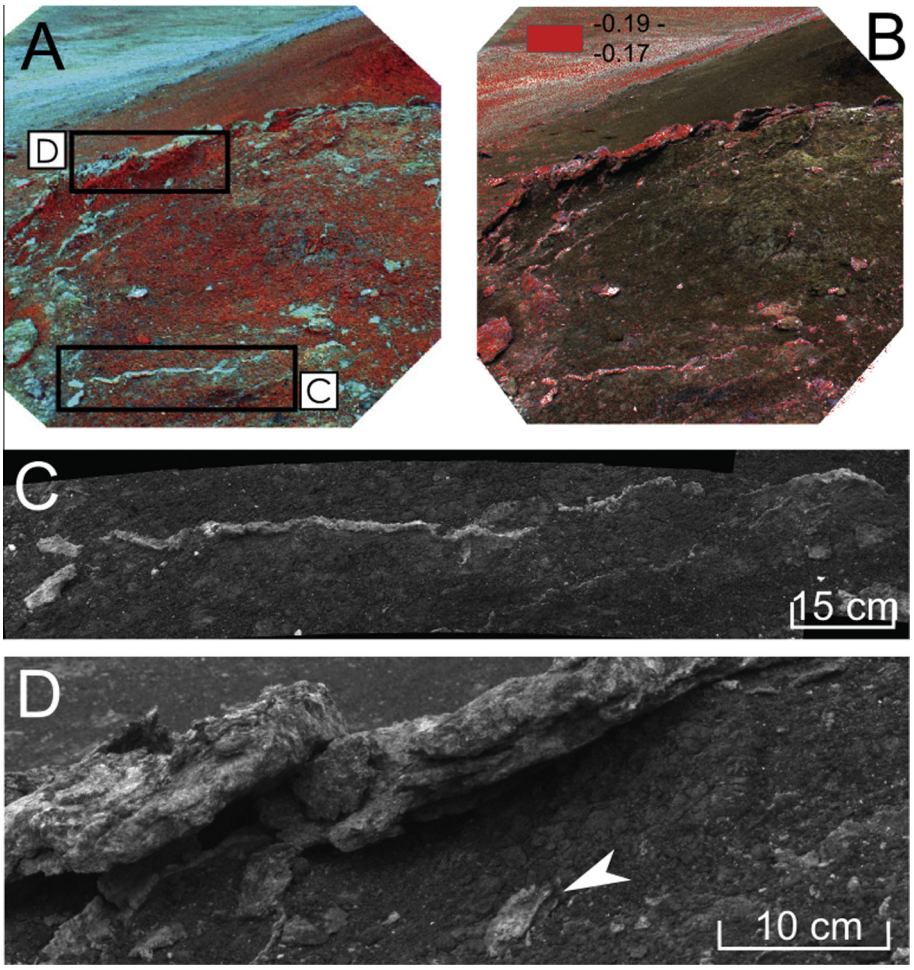

Fig. 9. AUPE-2 datasets for site A08_Vein. (A) False colour image (R = R/B ratio, G = R, B = G) showing distribution of mineral veins in the dark red unit; (B) LWAC spectral parameter image of the green slope (S532_610) minus the blue to red slope (S438_671) highlighting the mineral veins; (C and D) HRC monochrome mosaics of mineral veins, arrow shows a mineral vein fragment that has been weathered out of the original vein. (For interpretation of the references to colour in this figure legend, the reader is referred to the web version of this article.)

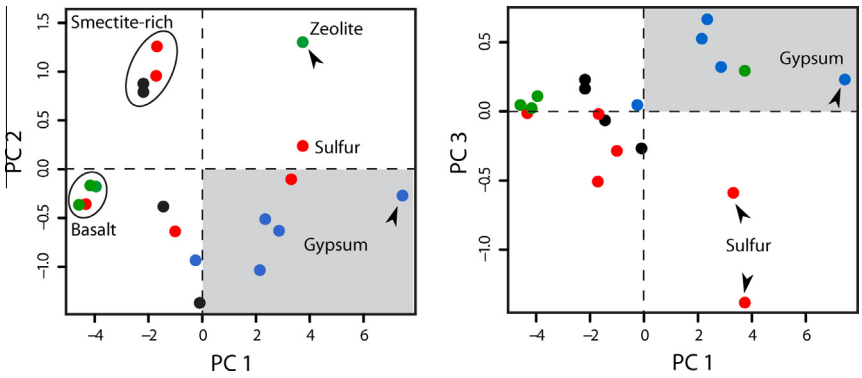

Fig. 10. Principal Component Analysis plots showing the groupings of spectral classes as observed with AUPE-2 R^* data. Vertical lines divide Fe-oxide bearing targets from high albedo non-Fe oxide targets including gypsum, zeolite, and sulfur. Horizontal lines further define the quadrant for which all gypsum-bearing targets fall within (grey box). Plots include all ROIs from sites A04_Tuff (black), A06_Soils (red), A07_Pillow (green), and A08_Vein (blue). (For interpretation of the references to colour in this figure legend, the reader is referred to the web version of this article.)

ROIs from the pillow basalts, which were identified as lithified volcaniclastics and weathered basalts respectively. High albedo ROIs with compositions of gypsum (ROI A08_001), zeolite (ROI A07_001) and sulfur (ROIs A06_002 and A06_004) are distinct from both basaltic/volcaniclastic lithologies and the Fe-oxide and phyllosilicate-bearing alteration soils. Gypsum-containing ROIs in particular all cluster within one distinct quadrant in both PCA plots. This finding corresponds well with recent work by Farrand et al. (2014) who found that gypsum veins on Cape York imaged by Opportunity proved spectrally distinct from other identified rock classes.

4.6. WAC performance

4.6.1. WAC field of view limitations

The WACs are separated by a distance of 50 cm laterally along the optical bench, to allow the acquisition of stereo images and subsequent 3D rendering of a target. However, while this provides vital structural information, this means that the two WACs are not viewing exactly the same scene – there are regions in the LWAC FoV that do not fall within the RWAC FoV and vice versa. This is an issue that has been faced by all stereo cameras on previous rover missions, however in the case of the ExoMars PanCam, this baseline separation of the WACs is significantly higher: 50 cm compared to 30 cm used for the MER Pancam (Bell et al., 2003). In addition, slight vignetting from the multispectral narrowband filters in the AUPE-2 system leads to unusable data in the corners once the images have been converted into R^* values (e.g. Fig. 6D and E), which will not be an issue for the ExoMars PanCam. The final percentage of the scene that is covered by both WACs and gives usable, calibrated multispectral reflectance data is approximately 85%, although this varies with target distance. The use of multiple frames to build up a panorama can go some way to alleviating this lack of overlap.

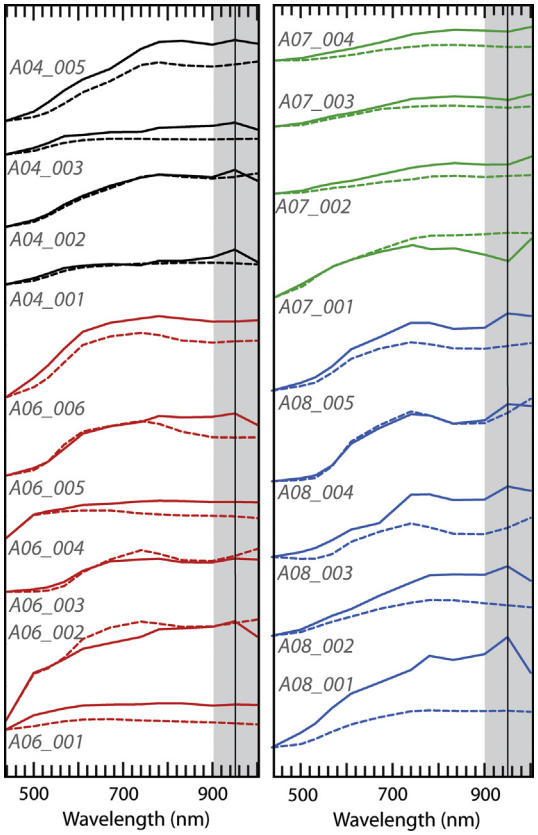

Fig. 11. Comparison of AUPE-2 R^* spectra (solid line) with *in situ* field spectrometer ROI measurements resampled to AUPE-2 spectral bands (dashed line). Solid vertical line represents the centre wavelength of the AUPE-2 950 nm filter, and grey region highlights the NIR region where hydration absorption features would be found (Rice et al., 2010).

4.6.2. Spectral discrepancy in the WAC NIR narrowband filters

Spectral ground-truthing of ROI AUPE-2 data reveals significant discrepancies between the R^* reflectance values and the corresponding reflectance spectra acquired using the *in situ* field spectrometer under comparable sampling conditions (Fig. 11). The most severe discrepancies were observed in the NIR, and particularly at the 950 and 1000 nm filters, which often produced a negative 'absorption' slope to 1000 nm or a slight absorption band at 950 nm that was not present in the field spectrometer data. Overall, AUPE-2 R^* and corresponding reflectance spectra from all sites can be classified as follows: (i) consistent spectral profile/morphology but with differences in relative albedo (nine ROIs, e.g. A04_005), (ii) complete match (within error) except for the 950 nm values (three ROIs, e.g. A08_004), (iii) complete match (within error) in visible wavelengths but divergence in NIR wavelengths (three ROIs, e.g. A06_006), (iv) semi-matched profiles and albedos (two ROIs, e.g. A06_002), and (v) poor or highly inconsistent match (two ROIs, e.g. A08_003). The *in situ* field spectrometer results are consistent with the laboratory VNIR spectra taken from the intact original surfaces of the ROI samples, confirming their validity. Therefore the observed spectral discrepancies between

AUPE-2 R^* spectra and the ground-truth spectra are inferred to be genuine artefacts of the AUPE-2 system. Due to this we were unable to use any of the NIR spectral parameters listed in Table 2.

5. Discussion

5.1. Detection of past habitability

AUPE-2 was deployed at four discrete sites within a 1 km^2 area. Aerial spectral data covering this region suggested significant variation across small spatial scales and ground reconnaissance confirmed the validity of this below the resolution of the aerial imagery. The four sites were specifically selected based on the ground level mineralogical and structural variation they represented in order to comprehensively test flight-like PanCam data products. Overall, AUPE-2 data provided geological information regarding the size, colour, morphology, weathering state, oxidation, broad composition, and cm- to m-scale features of all outcrops. Of particular relevance to previously observed Mars surface geology are (i) the iron oxide- and smectite-rich mineral soils identified at sites A04_Tuff, A06_Soils, and A08_Vein, and (ii) secondary zeolite and gypsum mineral veins at sites A07_Pillow and A08_Vein respectively. The MER *Opportunity* and MSL *Curiosity* rovers have both discovered secondary mineralisation in the form of cross-cutting hydrated sulfate mineral veins (Squyres et al., 2012; Vaniman et al., 2014), and zeolites have been detected on Mars from orbit (Wray et al., 2009). Deployment of AUPE-2 at sites A07_Pillow and A08_Vein therefore enabled data products similar to those that will be collected by the ExoMars PanCam to be acquired from potentially similar deposits. The dominance of the alteration assemblage zeolite + montmorillonite + nontronite across all four sites is consistent with the low temperature (<150 °C) alteration of basaltic glass (Browne, 1978), coupled with discrete regions of higher (>150 °C) temperature alteration, yielding deposits of sulfur (Browne, 1978), such as those at site A06_Soils. The genetic relationship between major depositional and alteration events across all four sites could also be elucidated to some degree from the AUPE-2 datasets. From AUPE-2 data alone, it is possible to deduce that this environment was formed by an episode of subaqueous or subglacial volcanism emplacing pillow basalts (A07_Pillow) and volcaniclastic sediments (A04_Tuff) followed by at least two stages of low temperature hydrothermal alteration to produce widespread unconsolidated hydrated mineral soils (all sites) and later cross-cutting mineral veins (A07_Pillow and A08_Vein). Together, these imply the presence of significant liquid water or extensive ice (resulting in subaqueous or subglacial volcanism) and neutral–acidic pH alteration fluids. Of the four sites investigated, the gypsum veins at site A08_Vein and the smectite-rich soils at A08_Vein and A04_Tuff would be promising targets for further astrobiological investigation.

5.2. Data quality and limitations

5.2.1. Discrepancies between AUPE-2 and in situ spectrometer measurements

The most apparent flaw in the AUPE-2 multispectral data is the discrepancy between extracted R^* spectra derived from the multispectral image cube acquired with the WAC geology filters and the ground-truth *in-situ* reflectance spectra (Fig. 11). Discrepancies in albedo alone between AUPE-2 R^* and *in-situ* relative reflectance spectra are caused by differences in the viewing geometry between the two instruments. The AUPE-2 system viewed the ground plane at large angles, and the topography of the ground on the decimetre scale meant that regions of interest could vary from normal incidence to almost tangential to the camera axis. In contrast the integrating sphere contact probe on the Jaz field spectrometer was placed on the surface so that the measurements were always taken at 8°. At large angles most surfaces depart significantly from Lambertian behaviour and so differences in albedo are observed in the two measurements. Without knowing the bidirectional scattering distribution of the objects in each scene it is impossible to calculate absolute reflectance values, and so the values presented for all spectral measurements here are relative reflectance values. In every case either the incidence or emission angle of the AUPE-2 R^* data are different from the corresponding *in-situ* spectral measurements and so a perfect match in albedo of the coincident datasets is not to be expected.

Non-albedo differences are most evident in the NIR filters, with consistently unreliable R^* values extracted from the 950 and 1000 nm multispectral data which often produced a false 'absorption' at either 950 or 1000 nm. Images taken with some NIR filters (780–1000 nm) showed concentric artefacts which contributed to the errors in data points at these wavelengths. These artefacts are ghost images caused by stray light reflected within the optical system. The appearance of these artefacts is due to a combination of the stray light performance of the lenses and the mechanism by which the light enters the optical system (described below). The loss of data from the NIR end of the spectral range available to AUPE-2 (and therefore potentially the ExoMars PanCam) is of particular importance due to the location of the H_2O and OH^- absorption bands around 950 nm (Rice et al., 2010). Given the utility of the 950–1000 nm absorption slope band parameter in identifying hydrated mineral species and mapping their distribution across a scene (Rice et al., 2010; Vaniman et al., 2014), it is imperative that this issue is resolved.

The origin of the stray light and ring artefacts observed was investigated by imaging a uniform light source integrating sphere illuminated with narrowband (~4 nm full width at half maximum) light from a tuneable light source (xenon lamp and monochromator). A full description of these investigations is beyond the scope of this publication and so only a brief description is given. Ring artefacts were observed in the images only for illumination wavelengths below the specified centre wavelength of the filters. This can be attributed to that fact that the transmission band of the interference filers is shifted to shorter wavelengths as the angle of incidence of the light at the filter is increased (Gunn et al., 2011; CVI Melles Griot). The short wavelength (below the filter nominal centre wavelength) light passing through the filters is scattered from the baffles inside the lens assembly, resulting in some light reaching the detector. Some of this light reaching the detector is absorbed, contributing to the detected signal, and some is reflected back through the lens and reaches the filter at nearer normal incidence. At this angle of incidence the filter is highly reflective to the shortwave light and so it is reflected back towards the detector. An optical cavity may therefore be formed between the planar surfaces of the filter and detector and so ghost images are formed at the image plane. The increasing effect of the stray light observed at longer wavelengths is attributed to the fact that the shift in transmission wavelength of the filters is proportional to the nominal centre wavelength of the filter. As such, the NIR filters allow a greater proportion of stray light into the optical system than the visible filters. Although the field of view and filters of the AUPE-2 WACs are representative of the PanCam WACs, the internal geometry of the cameras and optical designs of the lenses are not and the stray light scattering distribution within the PanCam WAC optical system is likely to be different. The optical design of the ExoMars PanCam WACs may make it easier to suppress the off axis stray light to prevent similar artefacts being observed, particularly in the NIR data. The stray light performance of representative flight hardware will therefore be investigated once breadboard models of the flight PanCam WACs are available. The narrower field of view

of similar camera systems such as the MER Pancams (16°) and Phoenix Surface Stereo Imager (13.8°) prevented them from suffering similar stray light issues.

5.2.2. Utility of PanCam data products

The engineering constraints on PanCam limit both the spectral range and resolution. Whilst research has been undertaken to identify the most efficient and flexible combination of narrowband 'geology' filters for hydrated mineral terrains (Cousins et al., 2012), subtle spectral features are inevitably missed and definitive identification of unique minerals is rarely achievable with the PanCam wavelength range alone. The combination of WAC colour context images, multispectral data and greyscale HRC images however was effective at capturing structural and spectral geological features present within the different outcrops imaged by AUPE-2. In particular, whilst multispectral information could not always lead to the identification of a specific mineral species, it proved essential in highlighting compositional units and structural features not visible in the colour images alone. This is demonstrated by the PCA plots (Fig. 10) which enable geological targets to be spectrally grouped, further contributing to the geological interpretation of the surrounding terrain, and also for revealing nearby astrobiological targets of interest (e.g. gypsum veins) that are more accessible to the rover. Effective capturing of subtle absorption bands at 532, 610, and 671 nm by the updated geology filters (Cousins et al., 2012) meant spectral differences within Fe-bearing targets could be detected, and distinguished from those targets comprising of non-Fe^{3+} bearing minerals. For the sites investigated, smectite-rich targets formed a separate spectral group distinct from targets comprising of iron-oxide rich alteration soils, or secondary mineral deposition (gypsum, sulfur, zeolite) (Fig. 10). Moreover, when compared to the ARSF aerial data of the region, AUPE-2 multispectral data revealed a much higher diversity of mineral terrains and lithologies. While unsurprising given the difference in spatial resolution, it highlights the potential geological variety that may exist locally within regions of hydrothermal alteration and the importance of using complementary datasets. Finally, WAC multispectral data was valuable not just for the identification of both discrete and large-scale compositional differences within hydrated mineral deposits, but also for highlighting structural/morphological geological features. In some cases the multispectral data verified the structural features observed in WAC RGB mosaics, as with the pillow basalt structures at site A07_Pillow (Fig. 7C), while at site A04_Tuff finely layered bedding features in the volcaniclastic sediments were visible in multispectral data products alone (Fig. 5F). Sedimentary layering is a particularly important target for Mars surface exploration as it has been found in association with putative past habitable environments on Mars, such as that identified by MSL *Curiosity* at Gale Crater (Grotzinger et al., 2014).

Colour HRC images were not acquired due to the technical set up of AUPE-2 during the field deployment. However, the greyscale images provided adequate detail required for identification and analysis of features in the WAC field of view. This can be seen with the HRC mosaics of the gypsum veins at site A08_Vein and sub-metre structure of pillow basalts and cross-cutting zeolite veins at site A07_Pillow (Fig. 7E). These data were crucial for the verification and interpretation of these secondary mineral features, which for site A07_Pillow were approaching the limit of the WAC resolution. Through HRC verification of these fine cross-cutting mineral veins across the pillow basalt outcrop face, WAC multispectral false colour and spectral parameter mapping of these features could be interpreted with a higher degree of confidence. Due to the stereo configuration of the two WACs, PanCam also has the ability to acquire both greyscale and colour stereo data from which 3D images can be constructed. As with the HRC colour data, this aspect of PanCam was not investigated for this particular field test, but will be explored in future AUPE-2 field deployments.

The value of PanCam data lies in its acquisition of spatially-resolved information from whole outcrops and surrounding terrains. The contextual nature of this information means combining PanCam results with those from ExoMars analytical instruments that can identify specific mineral species (e.g. IR and Raman spectroscopy from drill samples, ISEM from remote targets) will yield the most promising results. As the majority of analytical instruments will be deployed *after* target selection, it is imperative that PanCam data can be used to identify and distinguish spectrally-distinct units so that analytical data can be extrapolated beyond the discrete sample acquired via the drill. This field test of AUPE-2 has demonstrated the ability of the ExoMars PanCam to achieve this objective, but so far only reliably using wavelengths within the visible spectral range.

6. Conclusions and future work

An ExoMars Panoramic Camera emulator was deployed at four individual sites across a ~1 km^2 region encompassing hydrothermal alteration of primary basaltic lithologies including hydrovolcanic lavas, volcaniclastic sediments, and subaerial lava flows. WAC multispectral data ground-truthed with *in-situ* reflectance spectra of the same target footprints revealed significant discrepancies in spectral profile in the NIR, highlighting the need to establish the reliability of multispectral data acquired with RWAC geology filters. Spectral parameter maps were crucial in highlighting both spectral and compositional diversity across a site, and also structural features such as sedimentary layering. The spectral parameters that were most valuable for this type of terrain were the narrowband red:blue ratio (R671/438), 610 nm band depth (BD610), and green–red slope (S532-610). Specifically for highlighting the gypsum veins at site A08_Vein, the green–red slope minus the blue–red slope (S532_610)–(S438_671) proved particularly effective. Overall, geological indicators of habitability reliably captured by PanCam-like data from this region include secondary mineral veins, alteration soils, and volcaniclastic sedimentary bedding.

Future field-testing of PanCam and analysis of resulting multispectral data products will evolve to incorporate other analytical techniques that have been shown to be valuable, including identification of spectral end-members via Spectral Mixture Analysis (Parente et al., 2009; Farrand et al., 2013) and hierarchical clustering (Farrand et al., 2013, 2014). Additionally, a further product of WAC data is the generation of 3D Digital Elevation Models (Paar et al., 2007) that can reveal overall outcrop morphology and large-scale internal structure. Together with multispectral WAC and HRC data, this information will be another crucial factor in the selection of drill targets and interpretation of the local geology. Likewise, the effect of viewing angle on the resulting multispectral datasets also needs to be fully investigated given the wide (50 cm) baseline between the two WACs. Further investigation of the stray light effects in the multispectral WAC images identified by this work will be undertaken once the breadboard versions of the PanCam WACs are available. Finally, future work will compare aerial hyperspectral data with field-based VNIR spectral datasets with the view to clarifying how best to combine ExoMars PanCam data with orbital hyperspectral data, such as that produced by CRISM.

Author contributions

Data acquisition and analysis was conducted by JKH, MMG, CRC, and PMG. Calibration and stray light measurements of the AUPE-2 system were performed by MMG and REC. Preparation of the

manuscript was conducted by CRC and JKH, with additional scientific and technical input from DPB, IAC, and AJC.

Acknowledgments

Fieldwork in Iceland was funded by the Department of Earth and Planetary Sciences, Birkbeck, University of London, The Geological Remote Sensing Group and the Earth and Space Foundation. JKH is funded by a Birkbeck University of London Graduate Teaching Assistantship. CRC is funded by a Royal Society of Edinburgh Personal Research Fellowship co-funded by Marie Curie Actions. The Aberystwyth research leading to these results has been funded by the UK Space Agency, ExoMars Panoramic Camera (PanCam) Grant Nos. ST/G003114/1, ST/I002758/1, STL001454/1, and the UK Space Agency CREST2 PanCam-2020 research Grant No. ST/L00500X/1. Additional Aberystwyth funding has come from The European Community's Seventh Framework Programme (FP7/2007-2013), Grant Agreement Nos. 21881 PRoVisG, 241523 PRoViScout, and Grant Agreement No. 312377 PRoViDE. PMG is funded by a UK Space Agency Aurora Fellowship (grants ST/J005215/1 and ST/L00254X/1). Data from the Natural Environment Research Council (NERC) ARSF are provided courtesy of NERC via the NERC Earth Observation Data Centre (NEODC). CRC acknowledges the loan of the ASD Fieldspec Pro (Ref: 661.1112) from NERC Field Spectroscopy Facility. Finally, we thank Mr. Steve Hirons at Birkbeck, University of London for providing XRD analysis, and the NASA/ESA Arctic Mars Analog Svalbard Expedition (AMASE), which enabled valuable field-testing of previous versions of AUPE-2 by the AMASE 2008–2013 PanCam teams. We thank the two anonymous reviewers for their helpful feedback and comments that improved this manuscript.

References

Amundsen, H.E.F. et al., 2010. Integrated ExoMars PanCam, Raman, and close-up imaging field tests on AMASE 2009. EGU General Assembly 2010 held 2–7th May in Vienna, Austria, p. 8757.

Anderson, R.B., Bell, J.F., 2013. Correlating multispectral imaging and compositional data from the Mars Exploration Rovers and implications for Mars Science Laboratory. Icarus 223, 157–180.

Ármannsson, H., 2005. Monitoring the effect of geothermal effluent from the Krafla and Bjarnarflag power plants on groundwater in the Lake Mývatn Area, Iceland, with particular reference to natural tracers. In: Proceedings World Geothermal Congress 2005, Antalya, Turkey, 24–29 April, 8p.

Arvidson, R.E. et al., 2014. Ancient aqueous environments at Endeavour Crater, Mars. Science 343, 1248097.

Barnes, D. et al., 2011. Multi-spectral vision processing for the ExoMars 2018 mission. In: 11th Symposium on Advanced Space Technologies in Robotics and Automation – ASTRA 2011, 12–14 April 2011, ESTEC, The Netherlands.

Bell III, J.F. et al., 2003. Mars Exploration Rover Athena Panoramic Camera (Pancam) investigation. J. Geophys. Res. - Planets 108 (E12), 8063.

Bishop, J.L. et al., 2008. Reflectance and emission spectroscopy of four groups of phyllosilicates: Smectites, kaolinite–serpentines, chlorites and micas. Clay Miner. 43, 35–54.

Bishop, J.L. et al., 2013. Coordinated analyses of Antarctic sediments as Mars analog materials using reflectance spectroscopy and current flight-like instruments for CheMin, SAM and MOMA. Icarus 224, 309–325.

Browne, P.R.L., 1978. Hydrothermal alteration in active geothermal fields. Annu. Rev. Earth Planet. Sci. 6, 229–250.

Carter, J. et al., 2013. Hydrous minerals on Mars as seen by the CRISM and OMEGA imaging spectrometers: Updated global view. J. Geophys. Res. – Planets 118, 831–858.

Cloutis, E.A., Asher, P.M., Mertzmann, S.A., 2002. Spectral reflectance properties of zeolites and remote sensing implications. J. Geophys. Res. – Planets 107, E9.

Coates, A.J. et al., 2012. Lunar PanCam: Adapting ExoMars PanCam for the ESA Lunar Lander. Planet. Space Sci. 74, 247–253.

Coradini, A. et al., 2001. MA_MISS: Mars multispectral imager for subsurface studies. Adv. Space Res. 28, 1203–1208.

Cousins, C.R., Crawford, I.A., 2011. Volcano–ice interaction as a microbial habitat on Earth and Mars. Astrobiology 11, 695–710.

Cousins, C.R. et al., 2010. Astrobiological considerations for the selection of the geological filters on the ExoMars PanCam instrument. Astrobiology 10, 933–951.

Cousins, C.R. et al., 2012. Selecting the geology filter wavelengths for the ExoMars Panoramic Camera instrument. Planet. Space Sci. 71, 80–100.

Cousins, C.R. et al., 2013. Mars analogue glaciovolcanic hydrothermal environments in Iceland: Detection and implications for astrobiology. J. Volcanol. Geotherm. Res. 256, 61–77.

CVI Melles Griot. Interference filters. In: CVI Melles Griot Technical Notes. Melles Griot®, IDEX Corporation, US.

Downs R.T., 2006. The RRUFF Project: An integrated study of the chemistry, crystallography, Raman and infrared spectroscopy of minerals. Program and Abstracts of the 19th General Meeting of the International Mineralogical Association in Kobe, Japan, pp. O03–O13.

Edwards, H.G.M., Hutchinson, I., Ingley, R., 2012. The ExoMars Raman spectrometer and the identification of biogeological spectroscopic signatures using a flight-like prototype. Anal. Bioanal. Chem. 404, 1723–1731.

Ehlmann, B.L. et al., 2008. Clay minerals in delta deposits and organic preservation potential on Mars. Nat. Geosci. 1, 355–358.

Ehlmann, B.L. et al., 2011. Subsurface water and clay mineral formation during the early history of Mars. Nature 479, 53–60.

Ehlmann, B.L. et al., 2012. Mineralogy and chemistry of altered Icelandic basalts: Application to clay mineral detection and understanding aqueous environments on Mars. J. Geophys. Res. 117, E00J16.

Ehlmann, B.L. et al., 2013. Geochemical consequences of widespread clay mineral formation in Mars' ancient crust. Space Sci. Rev. 174, 329–364.

Exelis Visual Information Solutions Inc., 2011. ENVI Version 4.8. <www.exelisvis.com>.

Farrand, W.H. et al., 2006. Spectral variability among rocks in visible and near infrared multispectral Pancam data collected at Gusev Crater: Examinations using spectral mixture analysis and related techniques. J. Geophys. Res. – Planets 111, E02S15.

Farrand, W.H. et al., 2007. Visible and near-infrared multispectral analysis of rocks at Meridiani Planum, Mars by the Mars Exploration Rover Opportunity. J. Geophys. Res. – Planets 112, E06S02.

Farrand, W.H. et al., 2008. Rock spectral classes observed by the Spirit rover's Pancam on the Gusev Crater plains and in the Columbia Hills. J. Geophys. Res. 113, E12S38.

Farrand, W.H. et al., 2013. VNIR multispectral observations of rocks at Cape York, Endeavour Crater, Mars by the Opportunity rover's Pancam. Icarus 225, 709–725.

Farrand, W.H. et al., 2014. Observations of rock spectral classes by the Opportunity rover's Pancam on northern Cape York and on Matijevic Hill, Endeavour Crater, Mars. J. Geophys. Res. – Planets 119, 2349–2369.

Grindrod, P.M. et al., 2012. Formation of an Hesperian-aged sedimentary basin containing phyllosilicates in Coprates Catena, Mars. Icarus 218, 178–195.

Grotzinger, J.P. et al., 2014. A habitable fluvio-lacustrine environment at Yellowknife Bay, Gale Crater, Mars. Science 343 (6169), 1242777.

Gudmundsson, A. et al., 2010. Exploration and utilization of the Námafjall high temperature area in N-Iceland. In: Proceedings World Geothermal Congress 2010, Bali, Indonesia, 25–29 April 2010.

Gunn, M.D. et al., 2011. A method of extending the capabilities of multispectral interference filter cameras. In: Hyperspectral Imaging Conference 2011, Glasgow, UK, 17–18 May 2011.

Huber, G., Stetter, K.O., 1991. *Sulfolobus metallicus*, sp. nov., a novel strictly chemolithoautotrophic thermophilic archaeal species of metal-mobilizers. Syst. Appl. Microbiol. 14, 372–378.

Hunt, G.R., Ashley, R.P., 1979. Spectra of altered rocks in the visible and near infrared. Econ. Geol. 74 (7), 1613–1629.

Hurowitz, J.A. et al., 2006. In situ and experimental evidence for acidic weathering of rocks and soils on Mars. J. Geophys. Res. 111, E02S19.

Korablev, O. et al., 2013. AOTF near-IR spectrometers for study of lunar and martian surface composition. EPSC Abstracts, vol. 8, EPSC2013-50-1, 2013. European Planetary Science Congress 2013.

Leroi, V., Bibring, J.-P., Berthe, M., 2009. Micromega/IR: Design and status of a near-infrared spectral microscope for in situ analysis of Mars samples. Planet. Space Sci. 57, 1068–1075.

Merriman, R.J., Peacor, D.R., 1999. Very low-grade metapelites; mineralogy, microfabrics and measuring reaction progress. In: Frey, M., Robinson, D. (Eds.), Low-grade Metamorphism. Blackwell Sciences Ltd., Oxford, pp. 10–60.

Michalski, J.R. et al., 2010. The Mawrth Vallis region of Mars: A potential landing site for the Mars Science Laboratory (MSL) mission. Astrobiology 10, 687–703.

Morris, R.V. et al., 2008. Iron mineralogy and aqueous alteration from Husband Hill through Home Plate at Gusev Crater, Mars: Results from the Mössbauer instrument on the Spirit Mars Exploration Rover. J. Geophys. Res. 113, E12S42.

Murchie, S.L. et al., 2009. A synthesis of martian aqueous mineralogy after 1 Mars year of observations from the Mars Reconnaissance Orbiter. J. Geophys. Res. – Planets 114, E00D06.

Paar, G. et al., 2007. Requirements and solutions for ExoMars rover Panoramic Camera 3D vision processing. Geophysical Research Abstracts, vol. 9, 03901, 2007, SRef-ID: 1607-7962/gra/EGU2007-A-03901.

Parente, M., Bishop, J.L., Bell, J.F., 2009. Spectral unmixing for mineral identification in Pancam images of soils in Gusev Crater, Mars. Icarus 203, 421–436.

Pugh, S. et al., 2012. AUPE – A PanCam emulator for the ExoMars 2018 mission. In: International Symposium on Artificial Intelligence, Robotics and Automation in Space.

Reid, R. et al., 1999. Imager for Mars Pathfinder (IMP) image calibration. J. Geophys. Res. – Planets 104 (E4), 8907–8925.

Rice, M.S. et al., 2010. Silica-rich deposits and hydrated minerals at Gusev Crater, Mars: Vis–NIR spectral characterization and regional mapping. Icarus 205, 375–395.
Rice, M.S. et al., 2013. Reflectance spectra diversity of silica-rich materials: Sensitivity to environment and implications for detections on Mars. Icarus 223, 499–533.
Schmidt, M.E. et al., 2009. Spectral, mineralogical, and geochemical variations across Home Plate, Gusev Crater, Mars indicate high and low temperature alteration. Earth Planet. Sci. Lett. 281, 258–266.
Schmidt, M.E. et al., 2014. Geochemical diversity in first rocks examined by the Curiosity rover in Gale crater: Evidence for and significance of an alkali and volatile-rich igneous source. J. Geophys. Res. – Planets 119, 64–81. http://dx.doi.org/10.1002/2013JE004481.
Schmitz, N. et al., 2010. The PanCam instrument on the 2018 ExoMars rover: Science implementation strategy and integrated surface operations concept. EGU General Assembly 2010 held 2–7th May in Vienna, Austria, p. 12138.
Schulze-Makuch, D. et al., 2007. Exploration of hydrothermal targets on Mars. Icarus 189, 308–324.
Squyres, S.W., Knoll, A.H., 2005. Sedimentary rocks at Meridiani Planum: Origin, diagenesis, and implications for life on Mars. Earth Planet. Sci. Lett. 250, 1–10.
Squyres, S.W. et al., 2012. Ancient impact and aqueous processes at Endeavour Crater, Mars. Science 336, 570–576.
Steininger, H. et al., 2012. Mars Organic Molecule Analyzer (MOMA) onboard ExoMars 2018. International Workshop on Instrumentation for Planetary Missions, held October 10–12, 2012 in Greenbelt, Maryland. LPI Contribution No. 1683, p. 1116.
Stroncik, N.A., Schmincke, H.-U., 2002. Palagonite – A review. Int. J. Earth Sci. (Geol. Runds.) 91, 680–697.
Vago, J. et al., 2006. ExoMars—Searching for life on the Red Planet. ESA Bull. 126 (2006), 16–23.
Vaniman, D.T. et al., 2014. Mineralogy of a mudstone at Yellowknife Bay, Gale Crater, Mars. Science 343 (6169), 1243480.
Viviano, C.E., Moersch, J.E., McSween, H.Y., 2013. Implications for early hydrothermal environments on Mars through the spectral evidence for carbonation and chloritization reactions in the Nili Fossae region. J. Geophys. Res. – Planets 118, 1858–1872.
Westall, F. et al., 2013. Habitability on Mars from a microbial point of view. Astrobiology 13 (9), 887–897.
Williams, R.M.E. et al., 2013. Martian fluvial conglomerates at Gale Crater. Science 340, 1068–1072.
Wray, J.J. et al., 2009. Diverse aqueous environments on ancient Mars revealed in the southern highlands. Geology 37, 1043–1046.